

# Universal control of superexchange in linear triple quantum dots with an empty mediator

Guo Xuan Chan,<sup>1</sup> Peihao Huang,<sup>2,3,4,\*</sup> and Xin Wang<sup>1,†</sup>

<sup>1</sup>*Department of Physics, City University of Hong Kong, Tat Chee Avenue,  
Kowloon, Hong Kong SAR, People's Republic of China,  
and City University of Hong Kong Shenzhen Research Institute,  
Shenzhen, Guangdong 518057, People's Republic of China*

<sup>2</sup>*Shenzhen Institute for Quantum Science and Engineering,  
Southern University of Science and Technology, Shenzhen, Guangdong 518055, People's Republic of China*

<sup>3</sup>*International Quantum Academy, Shenzhen, Guangdong 518048, People's Republic of China*

<sup>4</sup>*Guangdong Provincial Key Laboratory of Quantum Science and Engineering,  
Southern University of Science and Technology, Shenzhen, Guangdong 518055, People's Republic of China*

(Dated: March 30, 2022)

Superexchange is one of the vital resources to realize long-range interaction between distant spins for large-scale quantum computing. Recent experiments have demonstrated coherent oscillations between logical states defined by remote spins whose coupling is given by the superexchange interaction mediated by central spins. Excavating the potential of superexchange requires a full understanding of the interaction in terms of control parameters, which is still lacking in literature. Here, using full configuration interaction calculation, we study a linear triple-quantum-dot device in which the left and right dots are occupied by a single electron each, whose spin states define the computational basis states of a qubit. We have found that, when the detunings at the left and right dots are leveled, the superexchange can exhibit a non-monotonic behavior which ranges from positive to negative values as a function of the middle-dot detuning. We further show that the larger relative detuning between the left and right dots causes the magnitude of the superexchange to increase (decrease) for an originally positive (negative) superexchange. We then proceed to show that a much larger left-right dot detuning can switch the superexchange from an originally negative value at zero detuning to a positive one. Using a Hubbard-like model, we present analytical expressions of the superexchange and have found that they conform well qualitatively with the numerical results obtained from full configuration interaction calculations. Our results suggest that even a simple configuration of delocalized two-electron states in a linear triple-quantum-dot device exhibits superexchange energy with non-trivial behavior, making it a promising candidate for scaling up with various implementations.

## I. INTRODUCTION

The Heisenberg exchange interaction lays the foundation of spin-based quantum computation in semiconductor quantum-dots [1–19]. Utilizing the electrostatic nature of the electron configurations in quantum-dot arrays, exchange-based quantum gates offer tunability of the interaction strength, permitting universal quantum computation. However, exchange coupling only materializes for nearest-neighbor interactions, limiting the realization of large-scale quantum computing in which long-range interactions are desired.

To achieve scalable quantum computation, various coupling schemes for long-range interactions have been proposed, including capacitive Coulomb interaction [20–30], hybrid spin-cQED (circuit quantum electrodynamics) architectures which utilize couplings between electron spins and photons in microwave cavities [31–41] and the method of electron shuttling in which remote spins are physically brought closer to enable nearest-neighbor

exchange interaction [42–48]. The former two schemes suffer from susceptibility to charge noises due to the introduced dipole for the enhancement of coupling strength while the latter requires a careful pulse design to preserve spin and phase coherence during the shuttling operation [44, 48].

An alternative coupling scheme involves mediators formed by electron spin states between distant logical spins, termed as the superexchange [49–64]. Virtual exchange through mediators enables a long-range linkage between remote spins, giving rise to the superexchange interaction. Current experimental demonstrations on superexchange include single-quantum-dot mediators with various electron numbers (e.g. zero [57], one [62] or multiple electrons [59]) and singly-occupied quantum-dot chain [63]. Also, the spatial separation of logical spin states can potentially serve to mitigate crosstalk during the single-qubit operation [58].

Systematic studies on superexchange have been conducted for few configurations in which the interaction strength is measured in terms of control parameters, e.g. detunings [57, 61], nearest-neighbor exchange within the mediators or between the mediators and logical spins [63]. In particular, Ref. 57 has concluded that, in experiments based on a triple-quantum-dot (TQD) device with

\*Electronic address: [huangph@sustech.edu.cn](mailto:huangph@sustech.edu.cn)

†Electronic address: [x.wang@cityu.edu.hk](mailto:x.wang@cityu.edu.hk)

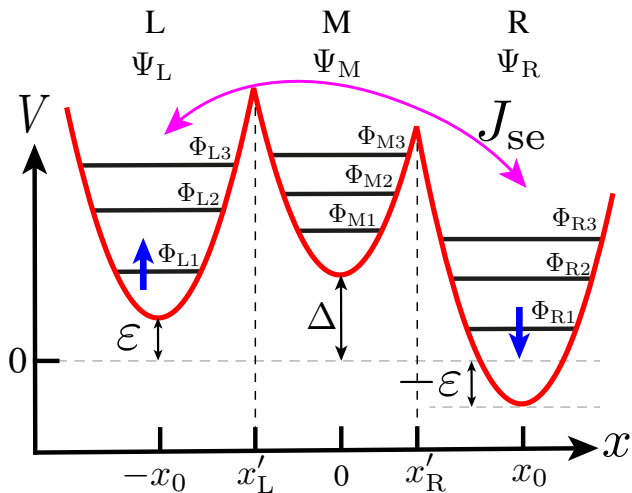


FIG. 1: Schematic illustration of a TQD device.  $\Phi_{\lambda j}$  indicates the  $j$ -th orthogonalized Fock-Darwin (F-D) states in dot  $\lambda$ , where  $\lambda \in \{L, M, R\}$ .  $\Psi_\lambda$  indicates the converged single-electron wavefunction in dot  $\lambda$ .  $J_{se}$  (magenta arrow) indicates the superexchange between dot L and R.

two electrons, superexchange between spins in singly-occupied outmost dots is monotonic with respect to the relative detuning between outmost dots. Also, Ref. 61, a theoretical work on superexchange in a triangular TQD, shows that the presence of an empty quantum-dot mediator contributes a modest enhancement to the direct exchange between two logical spins.

Although the aforementioned works are instrumental in understanding the mechanism of superexchange in quantum-dot devices, more comprehensive studies exploring superexchange in other regimes of parameters are still lacking. In this paper, using full Configuration Interaction (full CI) calculations, we study the superexchange in a linear TQD device in which the logical states are defined by two electron spins in the left and right dots while maintaining an empty middle dot. We will show that, when the left-right detuning  $\varepsilon$  is zero, the superexchange  $J_{se}$  yields a non-monotonic curve which switches from positive to negative values as a function of the middle-dot detuning  $\Delta$ . The switching sign of  $J_{se}$  is found to be present only for larger quantum-dot confinement strengths with smaller inter-dot distances. We will also show that when a sufficiently large left-right detuning  $\varepsilon$  is applied, an originally negative  $J_{se}$  switches to a positive value. We are able to understand the sign switching of  $J_{se}$  using a generic Hubbard model. Our results suggest that the superexchange, among other novel coupling schemes in multi-quantum-dot devices, may open a viable route for scalable quantum-dot quantum information processing.

This paper is organized as follows. In Sec. II, we provide the details of the TQD system of interest, including the full CI calculations to obtain relevant eigenvalues and eigenstates (Sec. II A) and the analytical expressions of  $J_{se}$  (Sec. II B). In Sec. III, we present the results under

different conditions: Sec. III A shows  $J_{se}$  as a function of the middle-dot detuning  $\Delta$  when the detuning between left and right dots is zero, i.e.  $\varepsilon = 0$ ; Sec. III B shows  $J_{se}$  for nonzero  $\varepsilon$ , i.e.  $\varepsilon > 0$ ; Sec. III C shows  $J_{se}$  as functions of  $\Delta$  and  $\varepsilon$ . We conclude our findings in Sec. IV.

## II. MODEL

### A. Configuration Interaction (CI)

We consider an  $n$ -electron system  $H = \sum h_j + H_C$  with the single-particle Hamiltonian  $h_j = (-i\hbar\nabla_j + e\mathbf{A}/c)^2/2m^* + V(\mathbf{r}) + g^*\mu_B\mathbf{B} \cdot \mathbf{S}$  and the Coulomb interaction  $H_C = \sum e^2/\epsilon|\mathbf{r}_j - \mathbf{r}_k|$ . As shown schematically in Fig. 1, the potential function of a triple-quantum-dot (TQD),  $V(\mathbf{r})$ , is modeled as

$$V(\mathbf{r}) = \begin{cases} V(\mathbf{r}|\mathbf{R}_L) + \varepsilon & x < -x'_L, \\ V(\mathbf{r}|\mathbf{R}_M) + \Delta & -x'_L < x < x'_R, \\ V(\mathbf{r}|\mathbf{R}_R) - \varepsilon & x > x'_R, \end{cases} \quad (1)$$

where

$$V(\mathbf{r}|\mathbf{R}) = \frac{1}{2}m\omega_0^2(\mathbf{r} - \mathbf{R})^2, \quad (2)$$

$\mathbf{r} = (x, y)$  is the two dimensional vector in the plane of electron gas.  $\mathbf{R}_L = (-x_0, 0)$ ,  $\mathbf{R}_M = (0, 0)$  and  $\mathbf{R}_R = (x_0, 0)$  are the positions of the parabolic wells minima.  $x'_L$  ( $x'_R$ ) is the potential cut determined by locating the value of  $x$  at which the potential values of left (right) and middle dot are equal at  $y = 0$ .  $\Delta$  and  $2\varepsilon$  are the middle-dot detuning and the relative detuning between the left and right dots respectively. The effective mass  $m^*$  is 0.067 electron mass in GaAs.  $\omega_0$  is the confinement strength.  $\mathbf{B} = B\hat{\mathbf{z}}$  is the perpendicular magnetic field and  $\mathbf{S}$  is the total electron spin. Throughout this work, the magnetic field is set at  $B = 0.845$  T. The charge configuration of the electrons in the TQD is denoted as  $(N_L, N_M, N_R)$ , where  $N_j$  indicates the electron number in dot  $j$ .

We solve the problem using the full CI technique. In full CI calculations, starting from the ground configuration of a multi-electron system, one increases the number of orbitals in the calculations until the results converge [65]. Before we present the numerical results of full CI, we first obtain an analytical result of  $J_{se}$  based on the generic Hubbard model [66], as shown in the following section.

### B. Analytical analysis of $J_{se}$

For a two-electron system hosted in a TQD,  $J_{se}$  is defined as the energy splitting between the lowest singlet and triplet states in the  $(N_L N_M N_R) = (101)$  region.

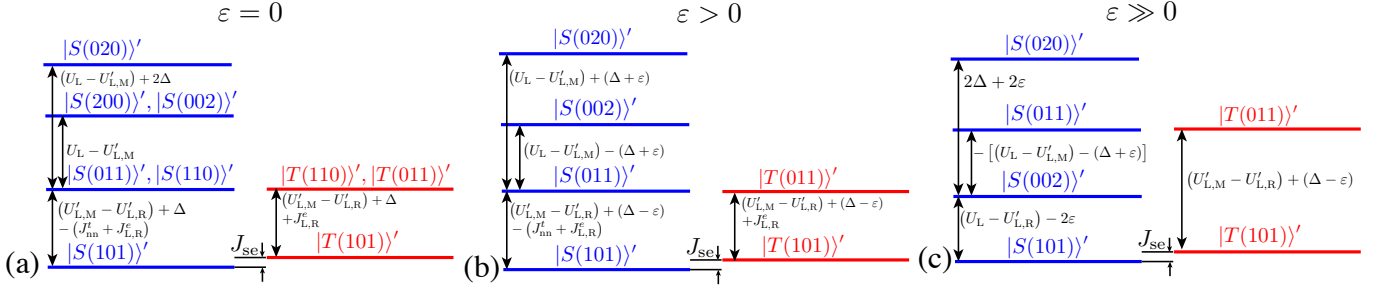


FIG. 2: Energy level structures of the system for (a)  $\varepsilon = 0$ , (b)  $\varepsilon > 0$  and (c)  $\varepsilon \gg 0$ . The Hubbard parameters are defined in Appendix B.

We use the notation  $|\eta\rangle'$  to denote an eigenstate whose main composition is  $|\eta\rangle$ . Also, the energy of state  $|\eta\rangle$  is denoted as  $E_{|\eta\rangle}$ . With the notations defined above,

$$J_{\text{se}} = E_{|T(101)\rangle'} - E_{|S(101)\rangle'}.$$

Using the generic Hubbard model [66] (see Appendix B for details),  $J_{\text{se}}$  as functions of  $\Delta$  and  $\varepsilon$  gives

$$J_{\text{se}}(\Delta, \varepsilon) \approx \begin{cases} \hat{J}_{\text{se}(L,M)}^t(\Delta, \varepsilon) \times J_{\text{nn}}(\Delta, \varepsilon) - 2J_{L,R}^e E_{|S(002)\rangle'} > E_{|S(011)\rangle'} > E_{|S(101)\rangle'} & \text{in (101) region,} \\ J_{\text{se}(L,M)}^t(\Delta, \varepsilon \gg 0) - 2J_{L,R}^e & E_{|S(011)\rangle'} > E_{|S(002)\rangle'} > E_{|S(101)\rangle'} & \text{in (101) region,} \end{cases} \quad (3a)$$

where

$$J_{\text{nn}}(\Delta, \varepsilon) = J_{\text{nn}}^t(\Delta, \varepsilon) - 2J_{L,M}^e, \quad (4a)$$

$$J_{\text{nn}}^t(\Delta, \varepsilon) = 2(t'_{L,M})^2 \xi_{\text{nn}}(\Delta, \varepsilon), \quad (4b)$$

$$\hat{J}_{\text{se}(L,M)}^t(\Delta, \varepsilon) = \left(\sqrt{2}t'_{L,M}\right)^2 \xi_{\text{se}}(\Delta, \varepsilon), \quad (4c)$$

$$J_{\text{se}(L,M)}^t(\Delta, \varepsilon \gg 0) \propto \Phi_{|S(002)\rangle'} + (\Phi_{|S(011)\rangle'} - \Phi_{|T(011)\rangle'}). \quad (4d)$$

In Eq. (3a), (3b) and (4), we denote the terms with the unit of energy as  $J$  with subscripts and superscripts indicating their characteristics, while the terms without unit, i.e. the normalized terms, with an over-hat symbol,  $\hat{J}$ .

Figure 2 shows the energy level structures of the system under different conditions depicted in Eq. (3a) and Eq. (3b). In particular, Eq. (3a) shows the analytical expressions of  $J_{\text{se}}$  for  $\varepsilon = 0$  and  $\varepsilon > 0$ , which will be discussed in accordance with the numerical results in Sec. III A and Sec. III B 1 respectively. The energy level structures that are applicable to the former and the latter case are shown in Fig. 2(a) and (b) respectively. One can validate that Fig. 2(a) concurs with Fig. 3 while Fig. 2(b) concurs with Fig. 12 and Fig. 13. On the other hand, for  $\varepsilon \gg 0$ , the analytical expression of  $J_{\text{se}}$  is given in Eq. (3b), which will be adopted in the discussion of the numerical results in Sec. III B 2. Also, the structure of eigenstate energies for  $\varepsilon \gg 0$  is shown in Fig. 2(b), which concurs with those presented in Fig. 7 and Fig. 15.

The derivations of  $J_{\text{se}}$  are presented in Appendix F, where Appendix F 1-F 2 and Appendix F 3 provide the

derivations for Eq. (3a) and (3b) respectively.  $\xi_{\text{se}}$  and  $\xi_{\text{nn}}$  denote the effect of higher lying states on the eigenstates of interest, represented by inverses of energy differences, cf. Eqs. (5a), (5b), (6a) and (6b).

In contrast to the regions where  $\varepsilon = 0$  and  $\varepsilon > 0$ , in which the analytical expressions of  $J_{\text{se}}$  can be summarized in the same form, cf. Eq. (3a), a slightly more complicated analysis is required for the region where  $\varepsilon \gg 0$ . The region of  $\varepsilon \gg 0$  is defined when  $\varepsilon$  is sufficiently large such that  $E_{|S(011)\rangle'} > E_{|S(002)\rangle'} > E_{|S(101)\rangle'}$  in (101) region, cf. Fig. 2(c). Under this condition,  $J_{\text{se}}$  yields the form as shown in Eq. (3b) and Eq. (4d), whose derivation is provided in Appendix F 3. Eq. (4d) suggests that  $J_{\text{se}}$  in this regime can be made proportional to the admixture angles between different states.  $\Phi_{|S(N_L N_M N_R)\rangle'}$  denotes the degree of admixture between  $|S(101)\rangle'$  and  $|S(N_L N_M N_R)\rangle'$ . The same goes for  $\Phi_{|T(N_L N_M N_R)\rangle'}$ , cf. Eq. (7).

Eqs. (3a) and (3b) imply that  $J_{\text{se}}$  results from the interplay between the normalized tunneling induced term  $\hat{J}_{\text{se}(L,M)}^t(\Delta, \varepsilon \geq 0)$ , the virtual nearest-neighbor exchange term  $J_{\text{nn}}(\Delta, \varepsilon \geq 0)$ , the higher-order tunneling induced term  $J_{\text{se}(L,M)}^t(\Delta, \varepsilon \gg 0)$ , and the long-distance Coulomb exchange term between two outmost dots  $J_{L,R}^e$ . The aforementioned  $J_{\text{nn}}$  arises due to the tunnel coupling between the first excited singlet  $|S(011)\rangle'$  ( $|S(110)\rangle'$ ) and second excited singlet  $|S(002)\rangle'$  ( $|S(200)\rangle'$ ) states, cf. Fig. 2(a)-(b) and Appendix D 2. Although  $J_{\text{nn}}$  yields the same origin as the nearest-neighbor exchange of singly occupied dots in double-quantum-dot (DQD) devices, it does not contribute directly to  $J_{\text{se}}$  as it occurs

within the subspace of higher energy eigenstates (hence the nomenclature “virtual nearest-neighbor exchange”). In analogy to singlet-triplet splittings of two-electron systems in DQD devices [66, 67],  $J_{\text{nn}}$  consists of two components, i.e. the nearest-neighbor tunneling term  $J_{\text{nn}}^t$  and nearest-neighbor Coulomb exchange  $J_{L,M}^e$ , cf. Eq. (4a). Also, it is helpful to perceive  $J_{\text{nn}} > 0$  and  $J_{j,k}^e > 0$ , as discussed in Appendix D 1. The argument for the positive sign of  $J_{\text{nn}}$  is applicable since large magnetic fields are not considered in this work [68, 69], while the positive  $J_{j,k}^e$  is verified using full CI calculations on a two-electron system in a DQD device, see Appendix D 1 b for details.

Eqs. (4b) and (4c) indicate that, in the range where  $\varepsilon$  is not large, the magnitude of  $J_{\text{nn}}^t$  and  $\hat{J}_{\text{se}(L,M)}^t$  are proportional to the inverse of energy separations between eigenstates of interest. Written explicitly, the definitions of  $\xi_{\text{nn}}$  and  $\xi_{\text{se}}$  are (see Appendix F 1-F 2 for details)

$$\xi_{\text{se}}(\Delta, \varepsilon) = \begin{cases} \left( \frac{1}{E_{|S(110;011)+} - E_{|S(101)\rangle}} \right)^2 & \varepsilon = 0, \\ \left( \frac{1}{E_{|S(011)\rangle} - E_{|S(101)\rangle}} \right)^2 & \varepsilon > 0, \end{cases} \quad (5a)$$

$$\xi_{\text{nn}}(\Delta, \varepsilon) = \begin{cases} \frac{2}{E_{|S(020)\rangle} - E_{|S(110;011)+}} & \varepsilon = 0, \\ + \frac{1}{E_{|S(200;002)+} - E_{|S(110;011)+}} & \\ \frac{2}{E_{|S(002)\rangle} - E_{|S(011)\rangle}} & \varepsilon > 0. \end{cases} \quad (6a)$$

In the regime where  $\varepsilon \gg 0$ , Eq. (4d) suggests that the strength of  $J_{\text{se}(L,M)}^t$  is directly proportional to the admixture angle  $\Phi_{|\eta\rangle}$ . The values of  $\Phi_{|\eta\rangle}$  can be derived from the composition of state  $|\eta\rangle$  in the eigenstate  $|\eta\rangle'$ , i.e.

$$\Phi_{|S(002)\rangle} \propto \tilde{\Phi}_{|S(002)\rangle} = |\langle S(002)|S(101)\rangle'|, \quad (7a)$$

$$\Phi_{|S(011)\rangle} \propto \tilde{\Phi}_{|S(011)\rangle} = |\langle S(011)|S(101)\rangle'|, \quad (7b)$$

$$\Phi_{|T(011)\rangle} \propto \tilde{\Phi}_{|T(011)\rangle} = |\langle T(011)|T(101)\rangle'|, \quad (7c)$$

where we denote the actual composition probabilities given by CI results with an overhead tilde while the admixture angles appearing in the analytical expressions of  $J_{\text{se}}$  without the overhead tilde, cf. Eq. (4d).

Before we close this section, we note that the analytical expressions of  $J_{\text{se}}$  presented here are rather complicated; however, in the next section (Sec. III) we will use these results to interpret the behavior of  $J_{\text{se}}$  obtained using full CI calculations.

### III. RESULTS

The numerical results of the system are obtained by keeping 10 orthonormalized Fock-Darwin (F-D) states in

each dot, resulting in a total of 30 F-D states in a TQD device for the CI calculation. As suggested by the convergence of superexchange energy  $J_{\text{se}}$  (see Appendix A for details), this setup is sufficient to accurately simulate a two-electron system in the TQD device. For illustration purposes, throughout this paper, we plot  $J_{\text{se}}$  with positive and negative values as solid and dashed lines respectively.

#### A. $J_{\text{se}}$ v.s. $\Delta$ at $\varepsilon = 0$

1. *Two limiting cases: (1)  $J_{\text{se}}$  switches sign in (101) region and (2)  $J_{\text{se}} < 0$  in (101) region*

We first discuss two limiting cases in terms of the behavior of superexchange  $J_{\text{se}}$ : (1) The sign of  $J_{\text{se}}$  switches from positive to negative as a function of  $\Delta$  in (101) region, cf. Fig. 3(b); (2)  $J_{\text{se}}$  is always negative as a function of  $\Delta$  in (101) region, cf. Fig. 3(h). Note that in Figs. 3(b) and (h),  $N_M \leq 10^{-1}$  such that the system is maintained in the region where  $(N_L N_M N_R) \approx (101)$ . For case (1), using dot parameters of  $\hbar\omega_0 = 25$  meV and  $x_0 = 30$  nm as an example, full CI results show that  $J_{\text{se}}$  is positive at small  $\Delta$  and decreases as a function of  $\Delta$ , cf. Fig. 3(b). Above certain value of  $\Delta$  ( $\Delta > 5$  meV),  $J_{\text{se}}$  switches to negative value and increases until it reaches a maximum (indicated by a black star), exhibiting a sweet spot. Beyond the sweet spot,  $J_{\text{se}}$  maintains a negative value and decreases in magnitude as  $\Delta$  increases. For case (2), using dot parameters of  $\hbar\omega_0 = 14$  meV and  $x_0 = 40$  nm as an example, cf. Fig. 3(h),  $J_{\text{se}}$  first increases in magnitude when  $\Delta$  increase, cf. Fig. 3(g). After passing a threshold  $\Delta$ , the magnitude of  $J_{\text{se}}$  decreases, exhibiting a sweet spot (indicated as a black star). Different from case (1),  $J_{\text{se}}$  is always negative in case (2). We proceed to provide an in-depth analysis regarding the behavior of  $J_{\text{se}}$  for case (1) in Sec. III A 2 and case (2) in Sec. III A 3.

#### 2. $J_{\text{se}}$ switches sign in (101) region

The value of  $J_{\text{se}}$  exhibits a non-trivial behavior due to the interplay between the virtual nearest-neighbor exchange  $J_{\text{nn}}$ , higher-order tunneling induced term  $\hat{J}_{\text{se}(L,M)}^t$  and long-distance Coulomb exchange term  $J_{L,R}^e$ , cf. Eq. (3a). The following discussion is made in reference to the results presented in the left panel of Fig. 3, i.e. Fig. 3(a)-(f).

It is helpful to start the discussion at large  $\Delta$  region ( $\Delta > 14.5$  meV). At large  $\Delta$ , the logical eigenstates,  $|S(101)\rangle'$  and  $|T(101)\rangle'$ , is substantially separated from higher-lying states, resulting in  $|S(101)\rangle' \approx |S(101)\rangle$  and  $|T(101)\rangle' \approx |T(101)\rangle$ , which gives  $J_{\text{se}} \approx E_{|T(101)\rangle} - E_{|S(101)\rangle} = -2J_{L,R}^e < 0$  (cf. Eq. (F1) in Appendix F 1). This can also be deduced from Eq. (3a) which gives  $J_{\text{se}} \approx -2J_{L,R}^e$  as  $\hat{J}_{\text{se}(L,M)}^t \approx 0$  due to  $\xi_{\text{se}} \approx 0$  (Eq. (4c)

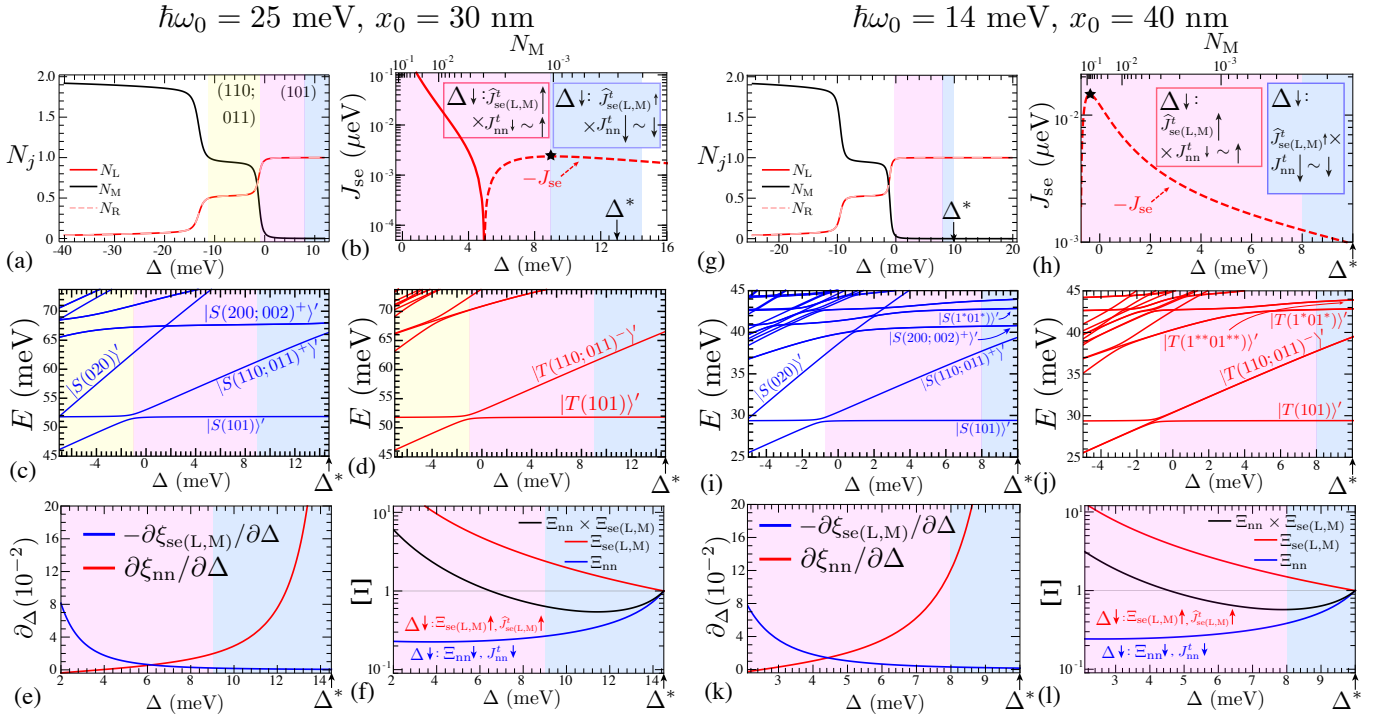


FIG. 3: Results of  $(N_L N_M N_R)$ ,  $J_{se}$ , eigenvalues of singlets and triplets,  $\partial\xi/\partial\Delta$  and  $\Xi$  v.s.  $\Delta$  obtained for  $\varepsilon = 0$  with dot parameters (a)-(f)  $\hbar\omega_0 = 25\text{meV}$ ,  $x_0 = 30\text{nm}$  and (g)-(l)  $\hbar\omega_0 = 14\text{meV}$ ,  $x_0 = 40\text{nm}$ . The dot occupations of ground eigenstates are denoted as  $(N_L N_M N_R)$ , with the yellow background indicates the hybridized region of (110) and (011), (110;011), while the magenta and blue backgrounds indicate the (101) region. (a), (g) Number of electrons occupying each dot,  $N_j$  for  $j \in \{L, M, R\}$ , v.s.  $\Delta$ . (b), (h) Superexchange energy  $J_{se}$  v.s.  $\Delta$  with positive and negative values plotted as solid and dashed lines respectively. The bottom axes label the  $\Delta$  values with the corresponding  $N_M$  values are labeled at the top axes. The arrows in the insets indicate the changes of  $\hat{J}_{se(L,M)}^t$  and  $J_{nn}^t$  with respect to  $\Delta$ , while the lengths of the arrows denote the magnitude of the changes. Lowest eigenvalues of singlets ((c), (i)) and triplets ((d), (j)) v.s.  $\Delta$ . (e), (k) The derivatives,  $-\partial\xi_{se}/\partial\Delta$  (blue line) and  $\partial\xi_{nn}/\partial\Delta$  (red line), v.s.  $\Delta$ . (f), (l)  $\xi_l$  v.s.  $\Delta$  with  $l \in \{nn, se(L,M)\}$ . The values are presented as ratios to those at  $\Delta = \Delta^*$ , i.e.  $\Xi_l(\Delta) = \xi_l(\Delta)/\xi_l(\Delta^*)$ .

and Eq. (5a)).

Next, we focus at the region of moderately large  $\Delta$ , i.e.  $9\text{ meV} < \Delta < 14.5\text{ meV}$  (the light blue background region). Fig. 3(b) shows that when  $\Delta$  decreases,  $J_{nn}^t$  decreases substantially while  $\hat{J}_{se(L,M)}^t$  slightly increases, as indicated by the statement in the box with light blue border. A fast decrease of  $J_{nn}^t$  and a slow increase of  $\hat{J}_{se(L,M)}^t$  with decreasing  $\Delta$  are suggested in Fig. 3(e), in which the derivatives with respect to  $\Delta$  are plotted. This is shown in more detail in Fig. 3(f), which shows that the overall decrease of  $\hat{J}_{se(L,M)}^t \times J_{nn}^t = (t'_{L,M})^4 \times \xi_{nn} \xi_{se}$  (black line) can be attributed to rapid change of  $\xi_{nn}$  (blue line) while a modest change of  $\xi_{se(L,M)}$  (red line). Note that the values of  $\xi_{nn}$  and  $\xi_{se(L,M)}$  are plotted as ratios to the values at  $\Delta = \Delta^*$ . It should be noted that the values of  $\xi_{nn}$  presented in Fig. 3(f) and Fig. 3(l) involve the contributions by both  $|S(020)\rangle$  and  $|S(200;002)^+\rangle$  (cf. Eq. (6a)), whose explicit values are given in Appendix C1b.

Lastly, we inspect the small  $\Delta$  region, i.e.  $0\text{ meV} < \Delta < 9\text{ meV}$ , as indicated by the magenta background. Fig. 3(b) shows that, starting from  $\Delta = 9\text{ meV}$ , when

$\Delta$  decreases, an initially negative  $J_{se}$  increases until it switches to positive  $J_{se}$ , which continues to increase for smaller  $\Delta$ . Fig. 3(f) (magenta background) shows that the increase of  $J_{se}$  with decreasing  $\Delta$  can be attributed to an overall increase of the term  $\hat{J}_{se(L,M)}^t \times J_{nn}^t = (t'_{L,M})^4 \times (\xi_{nn} \xi_{se})$  in which  $\xi_{se(L,M)}$  increases substantially while  $\xi_{nn}$  decreases slightly.

### 3. $J_{se} < 0$ in (101) region

Here we discuss the value of  $J_{se}$  which exhibits negative sign in all ranges of  $\Delta$  in (101) region, cf. the right panel of Fig. 3, i.e. Fig. 3(g)-(l). The qualitative behavior of negative  $J_{se}$  as a function of  $\Delta$  and its description based on the magnitude of  $\xi_{nn} \xi_{se}$  follows the discussions in the previous section, Sec. III A 2. However, a notable difference is that the turning point of the negative  $J_{se}$ , also a sweet spot (indicated as a black star), occurs at smaller  $\Delta$  as compared to the tuning point observed for  $\xi_{nn} \xi_{se}$  (black line in Fig. 3(l)). This is because more higher-lying states are brought closer to the first excited eigen-

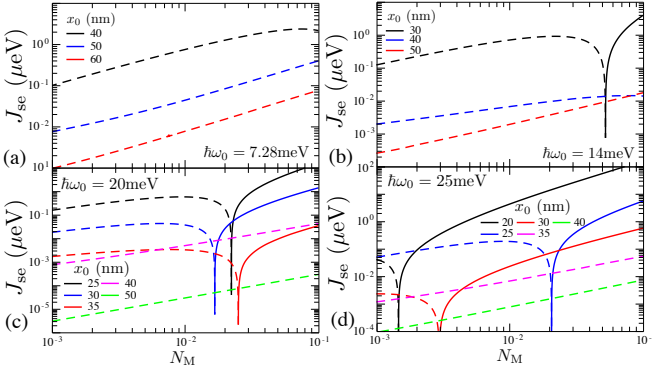


FIG. 4:  $J_{se}$  v.s.  $N_M$ , the electron number in dot M, for various inter-dot distances. The parameters are: (a)  $\hbar\omega_0 = 7.28$  meV, (b)  $\hbar\omega_0 = 14$  meV, (c)  $\hbar\omega_0 = 20$  meV and (d)  $\hbar\omega_0 = 25$  meV. The solid and dashed lines indicate  $J_{se} > 0$  and  $J_{se} < 0$  respectively.

states, i.e.  $|S(110;011)^+\rangle$  and  $|T(110;011)^-\rangle$  (compare Fig. 3(c) and (i) or (d) and (j)). Since, for analytical purposes, the expression of  $J_{se}$  presented in Eq. (3a) is obtained by truncating the generic Hubbard model into the lowest four singlet and two triplet eigenstates (see Appendix D 2 a and F 1 for details), the closeness between the low energy subspace and higher-lying states will result in the deviation of the sweet spot predicted by Eq. (3a). Nevertheless, the main qualitative behavior of  $J_{se}$  is well understood by inspecting the curves of  $\xi_{nn}$  and  $\xi_{se}$ , which are shown as blue and red line respectively in Fig. 3(1).

#### 4. $J_{se}$ for various inter-dot distances $x_0$ and confinement strengths $\hbar\omega_0$

Secs. III A 2 and III A 3 show two limiting cases of  $J_{se}$ , as exemplified by two sets of parameters, i.e.  $\hbar\omega_0 = 25$  meV,  $x_0 = 30$  nm and  $\hbar\omega_0 = 14$  meV,  $x_0 = 40$  nm. In this section, we continue to explore the behaviors of  $J_{se}$  for different pairs of  $\hbar\omega_0$  and  $x_0$ , as shown in Fig. 4. Note that, for comparison between different dot parameters, we plot the results as a function of electron number in middle dot  $N_M$ , which should be perceived as inversely proportional to  $\Delta$ . Hence, larger  $N_M$  (approaching the right side of each subfigure in Fig. 4) represents lower  $\Delta$ , and vice versa.

Figure 4 shows that, for fixed values of  $\hbar\omega_0$ , larger  $x_0$  has a tendency to yield negative  $J_{se}$  throughout the (101) region. As suggested by Eq. (3a), larger  $x_0$  gives smaller  $(t'_{L,M})^4$ . Hence effect of the term  $\hat{J}_{se(L,M)}^t \times J_{nn}^t$ , which causes  $J_{se}$  to switch from negative to positive values, is suppressed for larger  $x_0$ .

Also, Fig. 4 shows that smaller  $\hbar\omega_0$  has a tendency of exhibiting negative  $J_{se}$  in (101) region. Since a larger  $x_0$  is required to form a TQD confinement potential for a smaller  $\hbar\omega_0$ , the likelihood of the term  $\hat{J}_{se(L,M)}^t \times J_{nn}^t$  to

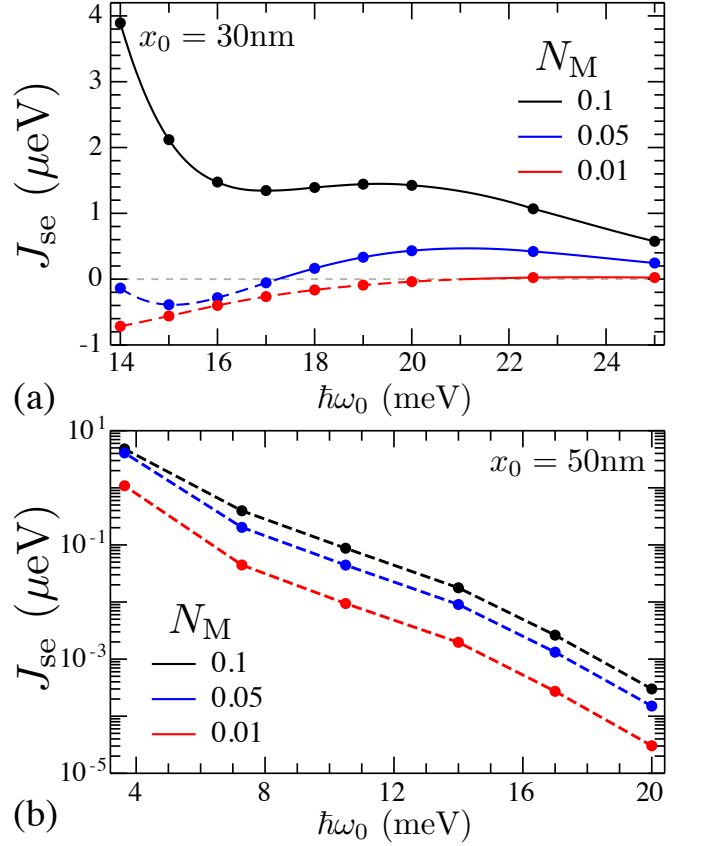


FIG. 5:  $J_{se}$  v.s. the confinement strength  $\hbar\omega_0$  for inter-dot distance (a)  $x_0 = 30$  nm and (b)  $x_0 = 50$  nm.  $J_{se}$  is plotted for fixed values of  $N_M$ , which the interpolated data points for  $N_M = 0.1$  (0.05, 0.01) are shown as a black (blue, red) line. The solid and dashed lines indicate  $J_{se} > 0$  and  $J_{se} < 0$  respectively.

compensate for the negative  $-2J_{L,R}^e$  is reduced. On the other hand, larger  $\hbar\omega_0$ , which favors smaller  $x_0$ , gives rise to the  $J_{se}$  that yields both positive and negative values as larger  $\hat{J}_{se}^t \times J_{nn}^t$  can be achieved.

Figure 5 presents  $J_{se}$  as a function of  $\hbar\omega_0$  under various  $x_0$  and  $N_M$ . For fixed values of  $x_0$  and  $N_M$ , Fig. 5(a) shows that an initially positive  $J_{se}$  at larger  $\hbar\omega_0$  switches to negative  $J_{se}$  at smaller  $\hbar\omega_0$ , cf. red and blue line, suggesting that  $\hat{J}_{se(L,M)}^t J_{nn}^t$  dominates at larger  $\hbar\omega_0$  while  $-2J_{L,R}^e$  dominates at small  $\hbar\omega_0$ . The same argument applies for Fig. 5(b) in which  $|J_{se}|$  yields larger magnitude for smaller  $\hbar\omega_0$ , suggesting a dominating value of  $-2J_{L,R}^e$  at small  $\hbar\omega_0$ . It should be made clear, for fixed values of  $x_0$ , that smaller  $\hbar\omega_0$  leads to larger values of  $\hat{J}_{se(L,M)}^t J_{nn}^t$  and  $-2J_{L,R}^e$  while the dominance of either term can be deduced from the resultant sign of  $J_{se}$ .

In addition, Fig. 5(a) shows that, for fixed values of  $\hbar\omega_0$  and  $x_0$  and in the range of  $10^{-2} < N_M < 10^{-1}$ , the positive  $J_{se}$  yields larger magnitude for larger  $N_M$ . Also, Fig. 5(b) shows that, in the range of  $10^{-2} < N_M < 10^{-1}$ , the negative  $J_{se}$  yields larger magnitude for larger

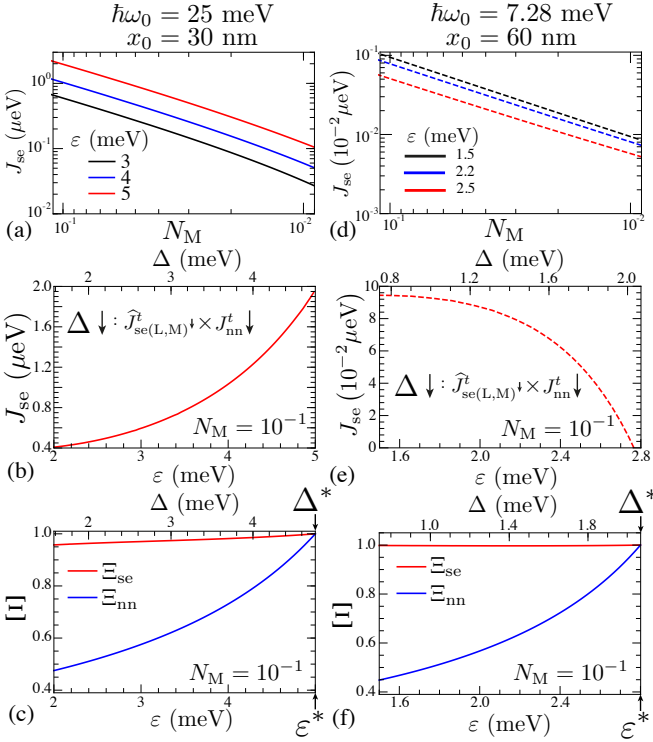


FIG. 6: Results of  $J_{se}$  and  $\Xi$  for (a)-(c)  $\hbar\omega_0 = 25$  meV,  $x_0 = 30$  nm and (d)-(f)  $\hbar\omega_0 = 7.28$  meV,  $x_0 = 60$  nm. (a), (d)  $J_{se}$  v.s.  $N_M$  for  $\varepsilon > 0$ . (b), (e)  $J_{se}$  v.s.  $\varepsilon$  for  $N_M = 10^{-1}$ . The arrows in the subfigures indicate the changes of  $J_{se}^t$  and  $J_{nn}^t$  with respect to  $\Delta$ , while the lengths of the arrows denote the magnitude of the changes. (c), (f)  $\xi_l$  v.s.  $\Delta$  with  $l \in \{se, nn\}$ .  $\xi_l$  is plotted as ratios to the values at  $\varepsilon = \varepsilon^*$  and  $\Delta = \Delta^*$ , i.e.  $\Xi_l(\Delta, \varepsilon) = \xi_l(\Delta, \varepsilon) / \xi_l(\Delta^*, \varepsilon^*)$ . The top axes in (b)-(f) indicate the corresponding  $\Delta$  to maintain  $N_M = 10^{-1}$ .

$N_M$ . These concur with the arguments made in previous sections, Sec. III A 2 and Sec. III A 3, in which the results show  $|J_{se}|$  yields larger magnitude for smaller  $\Delta$  (larger  $N_M$ ).

## B. $J_{se}$ v.s. $\Delta$ at $\varepsilon > 0$

### 1. $E_{|S(002)\rangle} > E_{|S(011)\rangle}$ in $(N_L N_M N_R) = (101)$ region

In this subsection, we consider  $J_{se}$  for  $\varepsilon > 0$  with the condition  $E_{|S(002)\rangle} > E_{|S(011)\rangle} > E_{|S(101)\rangle}$  satisfied. Figs. 12 and 13 in Appendix C 1 c confirm the above-mentioned condition is fulfilled for the range of  $\varepsilon$  considered here.

Figure 6 shows  $J_{se}$  when  $\varepsilon > 0$  for two sets of parameters, for which Fig. 6(a) gives positive  $J_{se}$  in (101) region (indicated as  $N_M < 10^{-1}$ ), while Fig. 6(d) gives negative  $J_{se}$  in (101) region. In Fig. 6(a) and (d),  $J_{se}$  is plotted as a function of  $N_M$ , which should be perceived as inversely proportional to  $\Delta$ .

Fig. 6(a) and (b) show that, for large  $\hbar\omega_0$  and small  $x_0$ ,

at fix values of  $N_M$ ,  $J_{se}$  is positive and exhibits stronger magnitude for larger  $\varepsilon$ . The increase of  $J_{se}$  as a function of  $\varepsilon$  can be attributed to the increase of  $\xi_{nn}$ , which results in the increase of  $J_{nn}$  (cf. Fig. 6(c) blue line), in accordance with Eq. (3a), Eq. (4b) and Eq. (6b). Although  $\hat{J}_{se(L,M)}^t$  also increases as a function of  $\varepsilon$ , represented as the increase  $\xi_{se}$  as a function of  $\varepsilon$ , cf. Fig. 6(c) (red line), the increase is limited compared to  $\xi_{nn}$ . Hence it can be derived that the increase of  $J_{se}$  with  $\varepsilon$ , while maintaining constant  $N_M$ , is dominated by the increase of  $J_{nn}$ .

On the other hand, Fig. 6(d) and (e) show that, for small  $\hbar\omega_0$  and large  $x_0$ , at fix values of  $N_M$ ,  $J_{se}$  is negative and exhibits smaller magnitude for larger  $\varepsilon$ . Based on Eq. (3a), Eq. (4b) and Eq. (6b), we can derive that the decrease of  $|J_{se}|$  as a function of  $\varepsilon$  can be attributed to the increase of  $\xi_{nn}$ . This results in the increase of  $J_{nn}$ ,

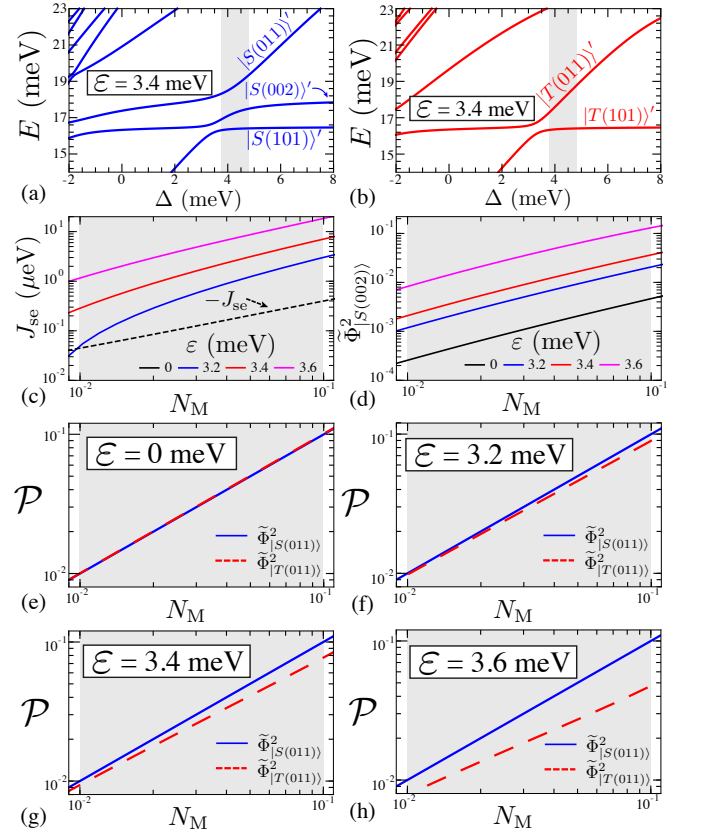


FIG. 7: Eigenvalues of (a) singlets (blue lines) and (b) triplets (red lines) v.s.  $\Delta$  for  $\varepsilon = 3.4$  meV. (c)  $J_{se}$  v.s.  $N_M$  for  $\varepsilon = 0$  meV (black line), 3.2 meV (blue line), 3.4 meV (red line) and 3.6 meV (magenta line). Solid and dashed lines indicate  $J_{se} > 0$  and  $J_{se} < 0$  respectively. (d) The composition of  $|S(002)\rangle$  in  $|S(101)\rangle$  ( $\tilde{\Phi}_{|S(002)\rangle}^2$ ) v.s.  $N_M$  for the values of  $\varepsilon$  given in (c). Note that, since  $E_{|S(200)\rangle} = E_{|S(002)\rangle}$  at  $\varepsilon = 0$ , the black line refers to  $|\langle S(200;002)^+ | S(101) \rangle|^2$ .  $\tilde{\Phi}_{|S(011)\rangle}^2$  (blue lines) and  $\tilde{\Phi}_{|T(011)\rangle}^2$  (red dashed lines) v.s.  $N_M$  for (e)  $\varepsilon = 0$ , (f) 3.2 meV, (g) 3.4 meV and (h) 3.6 meV. The dot parameters are:  $\hbar\omega_0 = 7.28$  meV,  $x_0 = 50$  nm.

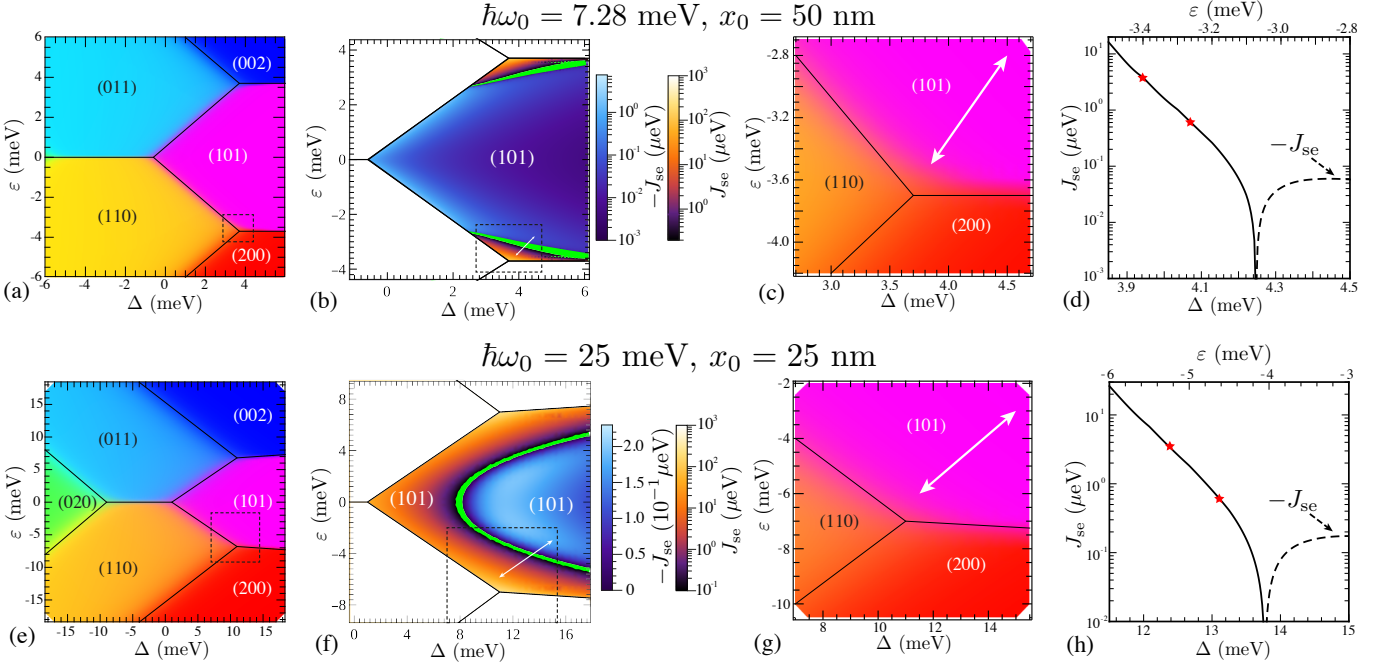


FIG. 8: Stability diagrams and  $J_{se}$  for (a)-(d)  $\hbar\omega_0 = 7.28$  meV,  $x_0 = 50$  nm and (e)-(h)  $\hbar\omega_0 = 25$  meV,  $x_0 = 30$  nm. (a), (e) Stability diagrams with the RGB color code defined as  $(128 \times N_L, 128 \times N_M, 128 \times N_R)$ . (b), (f)  $J_{se}$  v.s.  $\Delta$  and  $\varepsilon$  in (101) region. The green region marks the transition from  $J_{se} > 0$  to  $J_{se} < 0$ . (c) and (g) show the zoom in view of (a) and (e) respectively, as indicated by the dashed line boxes. (d), (h)  $J_{se}$  v.s.  $\Delta$  and  $\varepsilon$ . The pairings of  $\Delta$  and  $\varepsilon$  are given by the white double-headed arrows in (c) and (g). Two values of  $J_{se}$  demonstrated in Ref. 57 are presented as red stars.

hence reducing the difference,  $\hat{J}_{se(L,M)}^t J_{nn} - 2J_{L,R}^e$ . Similar to the arguments made in the previous paragraph, Fig. 6(f) (red line) shows that the increase of  $\hat{J}_{se(L,M)}^t J_{nn}$  is dominated by the increase of  $J_{nn}$  instead of  $\hat{J}_{se(L,M)}^t$ .

The same qualitative results can be derived for  $N_M = 10^{-2}$ , see Appendix C1d for details.

## 2. $E_{|S(011)\rangle} > E_{|S(002)\rangle}$ in $(N_L N_M N_R) = (101)$ region

Figure 7 compares  $J_{se}$  under two situations, i.e.  $\varepsilon = 0$  and  $\varepsilon \gg 0$ . The region of  $\varepsilon \gg 0$  is defined when  $\varepsilon$  is sufficiently large such that  $E_{|S(011)\rangle} > E_{|S(002)\rangle} > E_{|S(101)\rangle}$  in (101) region, cf. Fig. 7(a) (see Fig. 15 in Appendix C2 for eigenvalues of other  $\varepsilon$  values). Fig. 7(c) shows that  $J_{se}$  switches from negative to positive when  $\varepsilon$  is sufficiently large. Eq. (3b) argues that in  $\varepsilon \gg 0$  regime,  $J_{se}$  is a result of the interplay between  $J_{se(L,M)}^t$  and  $2J_{L,R}^e$ , while  $J_{se(L,M)}^t$  is directly proportional to the admixture angle  $\tilde{\Phi}_{|S(002)\rangle}$  and the difference of two angles  $\tilde{\Phi}_{|S(011)\rangle} - \tilde{\Phi}_{|T(011)\rangle}$ . As  $|S(101)\rangle'$  and  $|S(002)\rangle'$  are brought closer in energy by large  $\varepsilon$  (cf. Fig. 7(a) and Fig. 15 in Appendix C2),  $\tilde{\Phi}_{|S(002)\rangle}$  is enhanced (cf. Fig. 7(d)). Also, Fig. 7(e)-(h) show that the magnitude of  $\tilde{\Phi}_{|S(011)\rangle} - \tilde{\Phi}_{|T(011)\rangle}$  increases for larger  $\varepsilon$ . These

suggest that  $J_{se(L,M)}^t$  is substantially increased at large  $\varepsilon$ , which eventually results in the fact that the sign of  $J_{se}$  switches from negative to positive values, as shown in Fig. 7(c).

## C. Stability diagram and $J_{se}$ v.s. $\Delta$ and $\varepsilon$

Figure 8 shows the stability diagrams and the corresponding  $J_{se}$  as functions of  $\Delta$  and  $\varepsilon$  for two cases, i.e.  $\hbar\omega_0 = 7.28$  meV,  $x_0 = 50$  nm (Fig. 8(a)-(d)) and  $\hbar\omega_0 = 25$  meV,  $x_0 = 25$  nm (Fig. 8(e)-(h)). Two sets of parameters adopted here are qualitatively corresponding to results presented in Sec. III A and III B, as discussed in the following paragraphs.

For small  $\hbar\omega_0$ , i.e.  $\hbar\omega_0 = 7.28$  meV. Fig. 8(b) shows that, for small  $|\varepsilon|$  ( $|\varepsilon| < 2.8$  meV),  $J_{se}$  is negative in all the ranges of  $\Delta$  in (101) region. In contrast, for large  $\hbar\omega_0$  ( $\hbar\omega_0 = 25$  meV), Fig. 8(f) shows that  $J_{se}$  yields a transition from  $J_{se} > 0$  to  $J_{se} < 0$  as a function of  $\Delta$  for small  $|\varepsilon|$  ( $|\varepsilon| < 5.2$  meV). These concur with arguments presented for the two limiting cases in Sec. III A 1-III A 3 and the general results derived from different paired values of  $\hbar\omega_0$  and  $x_0$  in Sec. III A 4.

Fig. 8(b) shows that, for fixed values of  $\Delta$ , an initially negative  $J_{se}$  at small  $|\varepsilon|$  ( $|\varepsilon| < 2.8$  meV) switches to positive at large  $|\varepsilon|$  ( $|\varepsilon| > 2.8$  meV). The same results goes



for Fig. 8(f) for larger range of  $\Delta$  ( $\Delta > 8$  meV). These coincide with discussions presented in Sec. III B 2.

To compare our findings with experimental results,  $J_{se}$  is extracted along the double-headed white arrows as shown in Fig. 8(c) and (g), with the corresponding values of  $J_{se}$  provided in Fig. 8(d) and (h), respectively. Fig. 8(d) and (h) show that, within the part that gives  $J_{se} > 0$ ,  $J_{se}$  yields a monotonic decrease along the path given by the white arrows in Fig. 8(c) and (g), which includes the values of  $J_{se}$  demonstrated in Ref. 57. In Ref. 57, the detuning values closer to the triple-transition-point of (200), (110) and (101) region exhibits a strong  $J_{se}$  with magnitude  $\sim 3.75$   $\mu\text{eV}$  (900 MHz) while the detuning values away from the triple-transition-point exhibits a weak  $J_{se}$  with magnitude  $\sim 0.625$   $\mu\text{eV}$  (150 MHz). In the region where  $J_{se} > 0$ , the monotonic curves of  $J_{se}$  as a function of  $\varepsilon$  shown in Fig. 8(d) and (h) agree with results presented in Ref. 57.

#### IV. CONCLUSION AND DISCUSSION

We have shown, using full CI calculations, that the superexchange interaction, realized between two electrons which occupy two outmost dots individually in a TQD device, exhibits nontrivial behavior with respect to the control parameters. When  $\varepsilon = 0$ , symmetric TQDs with larger confinement strengths and shorter inter-dot distances yield  $J_{se}$  curves which are positive at small  $\Delta$  and switches to negative values at large  $\Delta$ . Also, the variations between positive and negative values of  $J_{se}$  are not monotonic, giving rise to sweet spots. Enabled by the crossing from positive  $J_{se}$  to negative  $J_{se}$ , the existence of zero value  $J_{se}$  is important to realize a *true* “turn off” of the exchange gate. Comparison of the numerical results of  $J_{se}$  for  $\varepsilon = 0$  to the analytical expression of  $J_{se}$  (Eq. (3a)) indicates that the non-monotonic behavior of  $J_{se}$  can be attributed to the interplay between the virtual nearest-neighbor exchange  $J_{nn}$  and the higher-order tunneling induced term  $\hat{J}_{se(L,M)}^t$ . Also, the sign switching behavior of  $J_{se}$  is found to be related to the competition between  $\hat{J}_{se(L,M)}^t \times J_{nn}$  and  $2J_{L,R}^e$ , the Coulomb exchange term between two outmost dots. For moderate  $\varepsilon$ , the

magnitude of  $J_{se}$  as a function of  $\varepsilon$  is largely influenced by  $J_{nn}$  which gives, at larger  $\varepsilon$ , larger magnitude of  $J_{se}$  for positive  $J_{se}$  and smaller magnitude of  $J_{se}$  for negative  $J_{se}$ . The contrasting behavior of the  $J_{se}$  strength for opposite signs of  $J_{se}$  stems from the negative sign of the Coulomb exchange term  $-2J_{L,R}^e$  in  $J_{se}$ . Entering the regime of large  $\varepsilon$ , we found that an originally negative  $J_{se}$  at  $\varepsilon = 0$  switches to yield positive values at large  $\varepsilon$ , which can be related to two reasons: (1) the enhanced admixture between the ground (101) singlet and (002) singlet; (2) larger admixture between the ground (101) singlet and (011) singlet compared to the same type of admixture between triplets. The switching between positive and negative  $J_{se}$  suggests this setup may serve as a quantum simulator when either antiferromagnetic interaction, ferromagnetic interaction or both are required [70–73].

Our results show that, depending on the quantum-dot and control parameters, superexchange interaction mediated by an empty quantum dot in a TQD device yields non-trivial behavior and ranges from positive to negative values, which may be harnessed to enhance the capabilities of spin qubits in quantum dots.

#### Acknowledgements

G.X.C. and X.W. are supported by the Key-Area Research and Development Program of Guangdong Province (Grant No. 2018B030326001), the National Natural Science Foundation of China (Grant No. 11874312), the Research Grants Council of Hong Kong (Grant No. 11303617), and the Guangdong Innovative and Entrepreneurial Research Team Program (Grant No. 2016ZT06D348). P.H. acknowledges supports by the National Natural Science Foundation of China (No. 11904157), Shenzhen Science and Technology Program (No. KQTD20200820113010023), and Guangdong Provincial Key Laboratory (No. 2019B121203002). The calculations involved in this work are mostly performed on the Tianhe-2 supercomputer at the National Supercomputer Center in Guangzhou, China.

#### Appendix A: Convergence

Since we are interested in evaluating the superexchange energy  $J_{se}$  for which the electron density in the middle dot is depleted, we define the procedure to achieve convergence as follows. Starting from 6 orbitals in each dot (a total of  $m = 18$  orbitals for a TQD device), the number of orbitals is simultaneously increased for the outmost dots (dot L and R) until it reaches 10 orbitals while maintaining 6 orbitals in dot M ( $m$  ranges from 18 to 26). The number of orbitals is then increased until it reaches 10 orbitals in dot M ( $m$  ranges from 27 to 30).

Figure 9 shows  $J_{se}$  as a function of  $\Delta$  for different number of orbitals  $m$  kept in full CI calculations. It can be observed that the main qualitative behavior emerges at  $m = 24$ . This is before the maximum number of orbitals in the outmost dots is reached, which  $m = 26$  (10 orbitals in outer dots and 6 orbitals in dot M). It can be observed that  $J_{se}$  approximately converges at  $m = 26$ . Further increasing the number of orbitals in dot M ( $m > 26$ ) provides a fine tuning for  $J_{se}$  until it converges at  $m = 29$ . Throughout this work, we keep 10 orbitals in all dots for full CI calculations, giving  $m = 30$ .

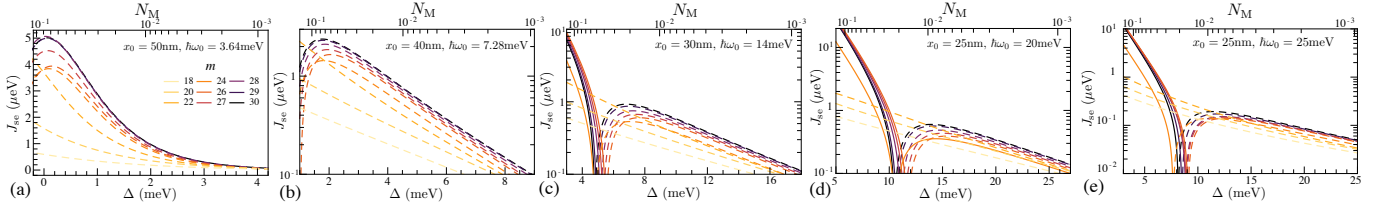


FIG. 9: Superexchange  $J_{se}$  v.s.  $\Delta$  for a given number of orbitals  $m$ . The color scheme is chosen such that  $J_{se}$  for the lowest number of orbitals ( $m = 18$ ) is plotted as yellow lines while  $J_{se}$  for the highest number of orbitals ( $m = 30$ ) is plotted as black lines, with the color gradient as a function of the orbital numbers  $m$  takes the path: yellow, orange, red and black. The parameters are: (a)  $x_0 = 50$  nm,  $\hbar\omega_0 = 3.64$  meV (b)  $x_0 = 40$  nm,  $\hbar\omega_0 = 7.28$  meV (c)  $x_0 = 30$  nm,  $\hbar\omega_0 = 14$  meV (d)  $x_0 = 25$  nm,  $\hbar\omega_0 = 20$  meV and (e)  $x_0 = 25$  nm,  $\hbar\omega_0 = 25$  meV.

## Appendix B: Generic Hubbard Model

The behavior of superexchange  $J_{se}$  can be well interpreted using the effective Hamiltonian derived from the generic Hubbard model [66], which includes all possible Coulomb interactions terms. The Hamiltonian is

$$\begin{aligned}
 H = & \sum_{j\sigma} \mu_{j\sigma} c_{j\sigma}^\dagger c_{j\sigma} + \sum_{j<k,\sigma} \left( t_{jk\sigma} c_{j\sigma}^\dagger c_{k\sigma} + \text{H.c.} \right) + \sum_j U_j n_{j\downarrow} n_{j\uparrow} + \sum_{\sigma\sigma'} \sum_{j<k} U'_{jk} n_{j\sigma} n_{k\sigma'} \\
 & - \sum_{\sigma\neq\sigma'} \sum_{j<k} J_{jk}^e c_{j\sigma}^\dagger c_{k\sigma'}^\dagger c_{k\sigma} c_{j\sigma} - \sum_{\sigma\neq\sigma'} \sum_{j<k} J_{jk}^p c_{j\sigma}^\dagger c_{j\sigma'}^\dagger c_{k\sigma} c_{k\sigma'} + \sum_{\sigma\neq\sigma'} \sum_{k<l} J_{j(k,l)}^t c_{j\sigma}^\dagger c_{j\sigma} c_{k\sigma'}^\dagger c_{l\sigma'},
 \end{aligned} \tag{B1}$$

where

$$\mu_j = \int d\mathbf{r}_j \Psi_j(\mathbf{r}) h \Psi_j(\mathbf{r}), \tag{B2a}$$

$$t_{j,k} = \int d\mathbf{r}_j \Psi_j(\mathbf{r}) h \Psi_k(\mathbf{r}), \tag{B2b}$$

$$U_j = \int d\mathbf{r}_1 d\mathbf{r}_2 \Psi_j^*(\mathbf{r}_1) \Psi_j^*(\mathbf{r}_2) H_C \Psi_j(\mathbf{r}_1) \Psi_j(\mathbf{r}_2), \tag{B2c}$$

$$U'_{j,k} = \int d\mathbf{r}_1 d\mathbf{r}_2 \Psi_j^*(\mathbf{r}_1) \Psi_k^*(\mathbf{r}_2) H_C \Psi_j(\mathbf{r}_1) \Psi_k(\mathbf{r}_2), \tag{B2c}$$

$$J_{j,k}^e = \int d\mathbf{r}_1 d\mathbf{r}_2 \Psi_j^*(\mathbf{r}_1) \Psi_k^*(\mathbf{r}_2) H_C \Psi_k(\mathbf{r}_1) \Psi_j(\mathbf{r}_2), \tag{B2d}$$

$$J_{j,k}^p = \int d\mathbf{r}_1 d\mathbf{r}_2 \Psi_j^*(\mathbf{r}_1) \Psi_j^*(\mathbf{r}_2) H_C \Psi_k(\mathbf{r}_1) \Psi_k(\mathbf{r}_2), \tag{B2e}$$

$$J_{j(k,l)}^t = \int d\mathbf{r}_1 d\mathbf{r}_2 \Psi_j^*(\mathbf{r}_1) \Psi_k^*(\mathbf{r}_2) H_C \Psi_j(\mathbf{r}_1) \Psi_l(\mathbf{r}_2), \tag{B2f}$$

$\{j, k, l\} \in \{L, M, R\}$  refer to the orbitals in left (L), middle (M) and right (R) dots respectively, while  $\sigma, \sigma'$  refer to the spins  $\{\sigma, \sigma'\} \in \{\uparrow, \downarrow\}$ . The summations over spins ( $\sigma, \sigma'$ ) are for up and down.  $\mu_{j\sigma}$  is the chemical potential of an electron with spin  $\sigma$  in dot  $j$ ,  $t_{jk\sigma}$  is the tunneling energy between dot  $j$  and  $k$ ,  $U_j$  is the on-site Coulomb interaction in dot  $j$ ,  $U'_{jk}$  is the inter-dot Coulomb interaction between dot  $j$  and  $k$ ,  $J_{jk}^e$  is the Coulomb exchange interaction between dot  $j$  and  $k$ ,  $J_{jk}^p$  is the two-electron co-tunneling energy from dot  $k$  to  $j$  and  $J_{j(k,l)}^t$  is the Coulomb assisted tunneling of an electron from dot  $l$  to  $k$  with another electron in dot  $j$ . The conditions  $j < k$  and  $k < l$  refers to the ordering from left to right, e.g. terms with  $j = L, k = M$  are allowed while  $j = M, k = L$  are dropped.

A two-electron Slater determinant formed by a spin-up electron occupying orbital  $j$  and a spin-down electron occupying orbital  $k$  is denoted as  $|\eta\rangle$ , where

$$\begin{aligned}
 |\eta\rangle &= |\uparrow_j \downarrow_k\rangle \\
 &= \frac{1}{\sqrt{2}} \begin{vmatrix} \Psi_j(\mathbf{r}_1) \uparrow(\omega_1) & \Psi_k(\mathbf{r}_1) \downarrow(\omega_1) \\ \Psi_j(\mathbf{r}_2) \uparrow(\omega_2) & \Psi_k(\mathbf{r}_2) \downarrow(\omega_2) \end{vmatrix}.
 \end{aligned} \tag{B3}$$

We denote the energy of  $|\eta\rangle$  as  $E_{|\eta\rangle}$ . The tunneling term between  $|\eta_1\rangle$  and  $|\eta_2\rangle$ ,  $\langle \eta_1 | H | \eta_2 \rangle$ , introduces energy shifts on

$E_{|\eta_1\rangle}$  and  $E_{|\eta_2\rangle}$ . Away from the avoided crossing between  $|\eta_1\rangle$  and  $|\eta_2\rangle$ , the energy shifts can be well approximated using Schrieffer-Wolff transformation [74]. The shifted eigenvalues are denoted as  $E_{|\eta\rangle'}$  with the corresponding eigenstates  $|\eta\rangle'$ , whose main composition is  $|\eta\rangle$ , i.e.  $\langle\eta|\eta\rangle' \approx 1$ .

Since the total spin operator  $\mathbf{S}^2$  commutes with the Hamiltonian  $H = \sum_j h_j + H_C$ , two-electron states with opposite spins ( $S_z = 0$ ) form two decoupled subspaces, one with  $S = 0$  and another one with  $S = 1$ , which are termed as ‘‘singlet’’ and ‘‘triplet’’ respectively. Correspondingly, the Slater determinants are denoted as

$$\begin{aligned} |S(\uparrow_j \downarrow_{k \neq j})\rangle &= \frac{1}{\sqrt{2}} (|\uparrow_j \downarrow_k\rangle + |\uparrow_k \downarrow_j\rangle), \\ |S(\uparrow_j \downarrow_j)\rangle &= |\uparrow_j \downarrow_j\rangle, \\ |T(\uparrow_j \downarrow_k)\rangle &= \frac{1}{\sqrt{2}} (|\uparrow_j \downarrow_k\rangle - |\uparrow_k \downarrow_j\rangle), \end{aligned} \quad (\text{B4})$$

for singlets ( $|S(\uparrow_j \downarrow_k)\rangle$ ) and triplets ( $|T(\uparrow_j \downarrow_k)\rangle$ ). The singlet and triplet states can also be identified by the electron occupation of the QDs, i.e.  $|S(N_L N_M)\rangle$  and  $|T(N_L N_M)\rangle$ , where  $N_j$  indicates the number of electrons occupying dot  $j$ . Some examples for two electrons in a DQD device are

$$\begin{aligned} |S(11)\rangle &= |S(\uparrow_L \downarrow_M)\rangle, \\ |S(20)\rangle &= |S(\uparrow_L \downarrow_L)\rangle, \\ |T(11)\rangle &= |T(\uparrow_L \downarrow_M)\rangle. \end{aligned} \quad (\text{B5})$$

Also, some examples for two electrons in a TQD device are

$$\begin{aligned} |S(101)\rangle &= |S(\uparrow_L \downarrow_R)\rangle, \\ |S(200)\rangle &= |S(\uparrow_L \downarrow_L)\rangle, \\ |T(110)\rangle &= |T(\uparrow_L \downarrow_M)\rangle, \end{aligned} \quad (\text{B6})$$

where  $|S(N_L N_M N_R)\rangle$  ( $|T(N_L N_M N_R)\rangle$ ) denotes a singlet (triplet) with  $N_j$  electrons in dot  $j$ .

In Eq. (B3)-(B6), two-electron Slater determinants are defined using the wavefunctions which give converged eigenvalues, i.e.  $\Psi_j$ . In some case, Slater determinants written in the bases of orthogonalized Fock-Darwin (F-D) states  $\Phi_j$  are mentioned in the discussions, which we will denote them as  $|\tilde{\eta}\rangle$ , such that

$$\begin{aligned} |\tilde{\eta}\rangle &= |\tilde{\uparrow}_j \tilde{\downarrow}_k\rangle \\ &= \frac{1}{\sqrt{2}} \begin{vmatrix} \Phi_j(\mathbf{r}_1) \uparrow(\omega_1) & \Phi_k(\mathbf{r}_1) \downarrow(\omega_1) \\ \Phi_j(\mathbf{r}_2) \uparrow(\omega_2) & \Phi_k(\mathbf{r}_2) \downarrow(\omega_2) \end{vmatrix}. \end{aligned} \quad (\text{B7})$$

Similarly, constructing two-electron singlets and triplets using orthonormalized F-D states gives

$$\begin{aligned} |\widetilde{S}(\uparrow_j \downarrow_{k \neq j})\rangle &= \frac{1}{\sqrt{2}} (|\tilde{\uparrow}_j \tilde{\downarrow}_k\rangle + |\tilde{\uparrow}_k \tilde{\downarrow}_j\rangle), \\ |\widetilde{S}(\uparrow_j \downarrow_j)\rangle &= |\tilde{\uparrow}_j \tilde{\downarrow}_j\rangle, \\ |\widetilde{T}(\uparrow_j \downarrow_k)\rangle &= \frac{1}{\sqrt{2}} (|\tilde{\uparrow}_j \tilde{\downarrow}_k\rangle - |\tilde{\uparrow}_k \tilde{\downarrow}_j\rangle), \end{aligned} \quad (\text{B8})$$

and

$$\begin{aligned} |\widetilde{S}(11)\rangle_{j,k} &= |\widetilde{S}(\uparrow_{Lj} \downarrow_{Mk})\rangle, \\ |\widetilde{S}(20)\rangle_{j,k} &= |\widetilde{S}(\uparrow_{Lj} \downarrow_{Lk})\rangle, \\ |\widetilde{T}(11)\rangle_{j,k} &= |\widetilde{T}(\uparrow_{Lj} \downarrow_{Mk})\rangle, \\ |\widetilde{S}(101)\rangle_{j,k} &= |\widetilde{S}(\uparrow_{Lj} \downarrow_{Rk})\rangle, \\ |\widetilde{S}(200)\rangle_{j,k} &= |\widetilde{S}(\uparrow_{Lj} \downarrow_{Lk})\rangle, \\ |\widetilde{T}(110)\rangle_{j,k} &= |\widetilde{T}(\uparrow_{Lj} \downarrow_{Mk})\rangle. \end{aligned} \quad (\text{B9})$$

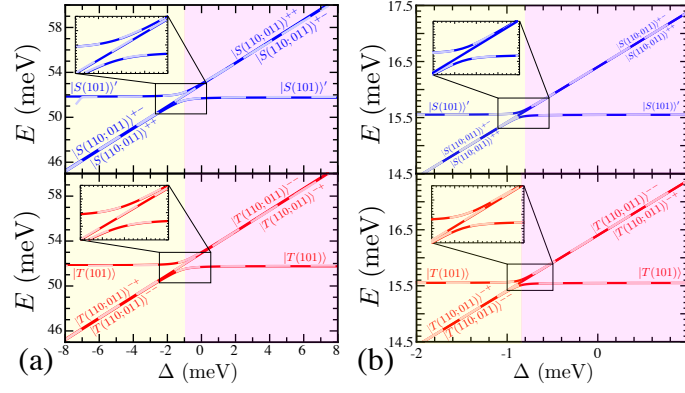


FIG. 10: Eigenvalues of lowest singlets (top row) and triplets (bottom row) v.s.  $\Delta$  for  $\varepsilon = 0$ . The parameters are: (a)  $\hbar\omega_0 = 25$  meV,  $x_0 = 30$  nm and (b)  $\hbar\omega_0 = 7.28$  meV and  $x_0 = 60$  nm. The solid lines are full CI results while the dashed lines are results from the generic Hubbard model. The Hubbard parameters are: (a)  $U'_{L,R} = 51.80$  meV,  $J_{L,R}^e = 2.39 \times 10^{-1}$   $\mu$ eV,  $2(J_{L,M}^e + t'_{L,R}) - J_{nn}^t = -4.81$   $\mu$ eV,  $U'_{L,M} - J_{nn}^t/2 = 52.90$  meV,  $t'_{L,M} = 255$   $\mu$ eV; (b)  $U'_{L,R} = 15.55$  meV,  $J_{L,R}^e = 5.77 \times 10^{-4}$   $\mu$ eV,  $2(J_{L,M}^e + t'_{L,R}) - J_{nn}^t = 0.86 \times 10^{-1}$   $\mu$ eV,  $U'_{L,M} - J_{nn}^t/2 = 16.40$  meV,  $t'_{L,M} = 33$   $\mu$ eV

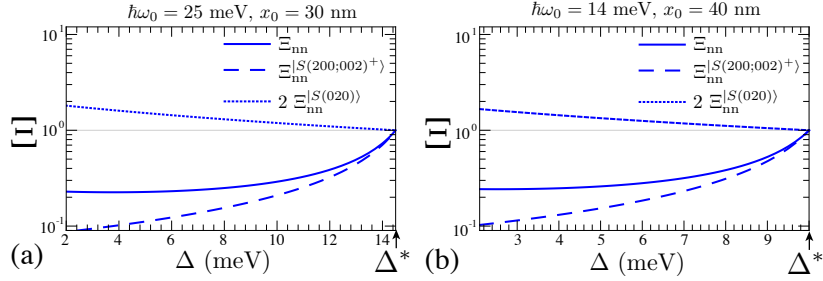


FIG. 11: Components of  $\xi_{nn}$ ,  $\xi_{nn}^{[S(200;002)^+]}$  and  $\xi_{nn}^{[S(020)]}$ , v.s.  $\Delta$ . The values are presented as ratios to those at  $\Delta = \Delta^*$ , i.e.  $\Xi_{nn}^{[\eta]}(\Delta) = \xi_{nn}^{[\eta]}(\Delta)/\xi_{nn}^{[\eta]}(\Delta^*)$  and  $\Xi_{nn}(\Delta) = \xi_{nn}(\Delta)/\xi_{nn}(\Delta^*)$ . The parameters are (a)  $\hbar\omega_0 = 25$  meV,  $x_0 = 30$  nm and (b)  $\hbar\omega_0 = 14$  meV,  $x_0 = 40$  nm.

## Appendix C: Supplemental figures which include additional information for discussions in the main text

### 1. Eigenvalues and eigenstates in the regime where $E_{|S(002)\rangle} > E_{|S(011)\rangle} > E_{|S(101)\rangle}$ in (101) region

#### a. Eigenvalues as a function of $\Delta$ at $\varepsilon = 0$ and their correspondence with Hubbard Model

Based on the effective Hamiltonian obtained using the generic Hubbard model (see Appendix B and Eq. (F4) for details), we can derive the quantitative values of  $t'_{L,M}$  by reproducing the eigenvalues of lowest singlets and triplets in (101) region and comparing them with full CI results. The reproduced eigenvalues are given in Fig. 10 (dashed lines). It can be observed that they conform with full CI results (solid lines).

#### b. Components of $\xi_{nn}$ v.s. $\Delta$ at $\varepsilon = 0$

Figure 11 shows  $\xi_{nn}$  as a function of  $\Delta$  at  $\varepsilon = 0$ . We denote the contribution of  $|S(020)\rangle$  and  $|S(200;002)^+\rangle$  states in the term  $\xi_{nn}$  as  $\xi_{nn}^{[S(020)]}$  and  $\xi_{nn}^{[S(200;002)^+]}$  respectively. The values of  $\xi_{nn}^{[020]}$  and  $\xi_{nn}^{[S(200;002)^+]}$ , together with  $\xi_{nn} = 2\xi_{nn}^{[020]} + \xi_{nn}^{[S(200;002)^+]}$ , are shown explicitly in Fig. 11.

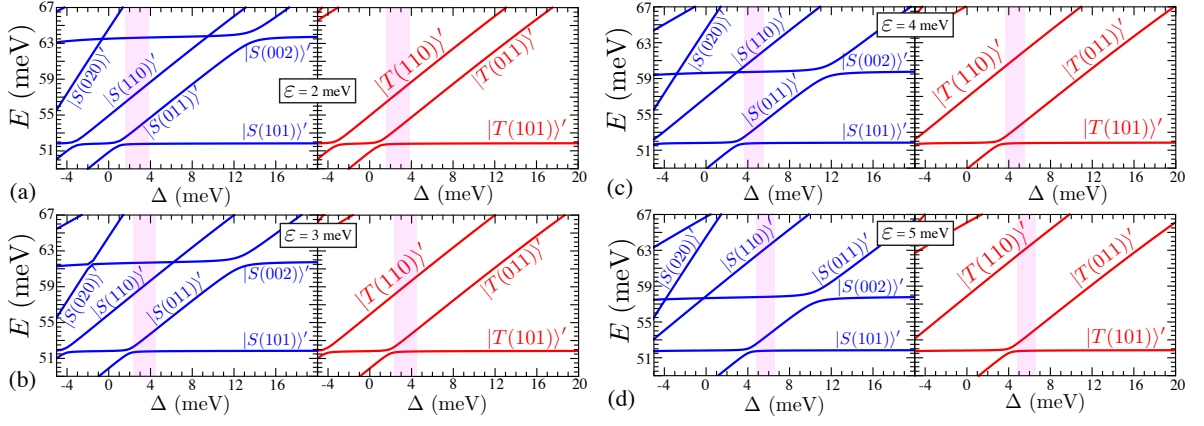


FIG. 12: Eigenvalues of singlets (blue lines) and triplets (red lines) v.s.  $\Delta$  for different values of  $\varepsilon$ , as indicated in the text boxes. The parameters are:  $\hbar\omega_0 = 25$  meV and  $x_0 = 30$  nm. The magenta background denotes the  $\Delta$  region in which  $N_M$  ranges from  $10^{-1}$  to  $10^{-2}$ . For each subfigure, the eigenvalues of singlets and triplets are plotted in the left and right panel respectively.

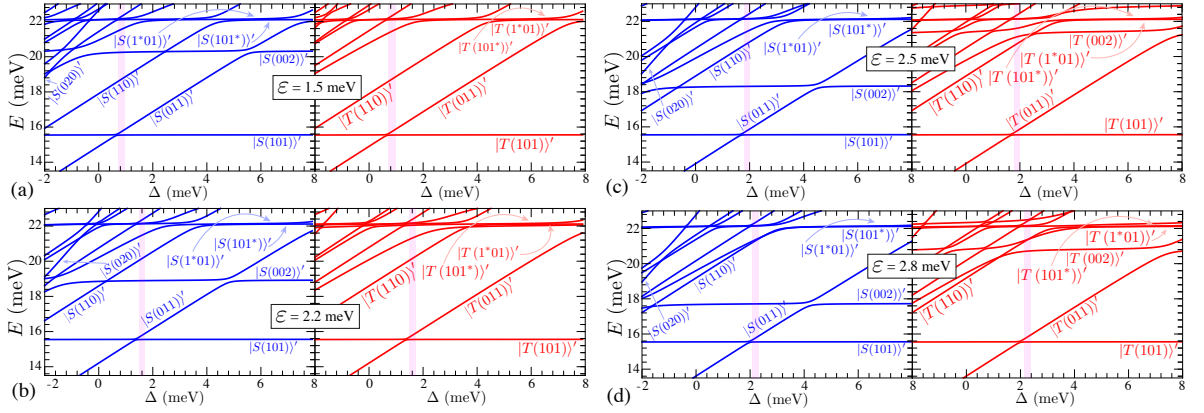


FIG. 13: Eigenvalues of singlets (blue lines) and triplets (red lines) v.s.  $\Delta$  for different values of  $\varepsilon$ , as indicated in the text boxes. The parameters are:  $\hbar\omega_0 = 7.28$  meV and  $x_0 = 60$  nm. The magenta background denotes the  $\Delta$  region in which  $N_M$  ranges from  $10^{-1}$  to  $10^{-2}$ . For each subfigure, the eigenvalues of singlets and triplets are plotted in the left and right panel respectively.

c. Eigenvalues v.s.  $\Delta$  for  $\varepsilon > 0$  which the condition  $E_{|S(002)\rangle} > E_{|S(011)\rangle} > E_{|S(101)\rangle}$  in (101) region is satisfied

Figure 12 shows the eigenvalues of singlets (blue solid lines) and triplets (red solid lines) as a function of  $\Delta$  for (a)  $\varepsilon = 2$  meV, (b)  $\varepsilon = 3$  meV, (c)  $\varepsilon = 4$  meV and (d)  $\varepsilon = 5$  meV, with the dots parameters as:  $\hbar\omega_0 = 25$  meV,  $x_0 = 30$  nm.

Figure 13 shows the eigenvalues of singlets (blue solid lines) and triplets (red solid lines) as a function of  $\Delta$  for (a)  $\varepsilon = 1.5$  meV, (b)  $\varepsilon = 2.2$  meV, (c)  $\varepsilon = 2.5$  meV and (d)  $\varepsilon = 2.8$  meV, with the dots parameters as:  $\hbar\omega_0 = 7.28$  meV,  $x_0 = 60$  nm.

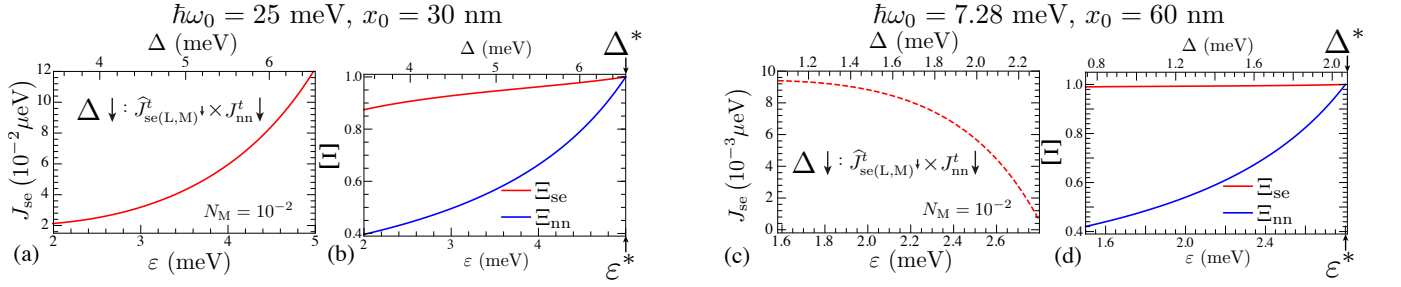


FIG. 14: Results of  $J_{se}$  and  $\Xi$  for (a)-(b)  $\hbar\omega_0 = 25$  meV,  $x_0 = 30$  nm and (c)-(d)  $\hbar\omega_0 = 7.28$  meV,  $x_0 = 60$  nm. (a) and (c) show  $J_{se}$  as functions of  $\epsilon$  (bottom axis) and  $\Delta$  (top axis). (b) and (d) show  $\xi_{nn}$  and  $\xi_{se}$  v.s.  $\epsilon$  (bottom axis) and  $\Delta$  (top axis).  $\xi_l$  is plotted as ratios to the values at  $\epsilon = \epsilon^*$  and  $\Delta = \Delta^*$ , i.e.  $\Xi_l(\Delta, \epsilon) = \xi_l(\Delta, \epsilon) / \xi_l(\Delta^*, \epsilon^*)$ , where  $l \in \{se, nn\}$ . The pairing of  $\epsilon$  and  $\Delta$  are fixed by maintaining  $N_M = 10^{-2}$ .

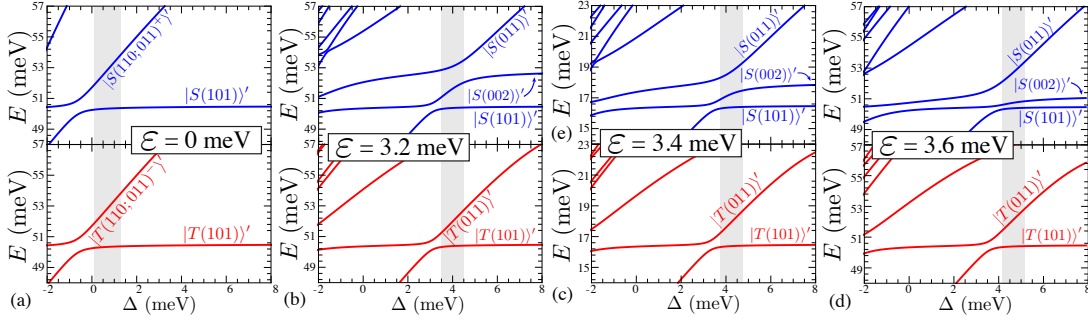


FIG. 15: Eigenvalues of singlets (blue lines) and triplets (red lines) v.s.  $\Delta$ . The results are obtained for  $\hbar\omega_0 = 7.28$  meV and  $x_0 = 50$  nm with (a)  $\epsilon = 0$  (b)  $\epsilon = 3.2$  meV, (c)  $\epsilon = 3.4$  meV and (d)  $\epsilon = 3.6$  meV. For each subfigure, the eigenvalues of singlets and triplets are plotted in the top and bottom panel respectively.

#### d. $J_{se}$ as functions of $\Delta$ and $\epsilon$ for $N_M = 10^{-2}$

Figure 14 shows  $J_{se}$ ,  $\xi_{nn}$  and  $\xi_{se}$  for two sets of parameters: (a)-(b)  $\hbar\omega_0 = 25$  meV,  $x_0 = 30$  nm and (c)-(d)  $\hbar\omega_0 = 7.28$  meV,  $x_0 = 60$  nm. The value of  $\Delta$  for a particular  $\epsilon$  is determined by maintaining  $N_M = 10^{-2}$ . The results show here yield the same qualitative behavior as Fig. 6(b), (c), (e) and (f), hence, the arguments in Sec. III B 1 are applicable here.

## 2. Eigenvalues in $\epsilon \gg 0$ regime where the condition $E_{|S(011)\rangle} > E_{|S(002)\rangle} > E_{|S(101)\rangle}$ in (101) region is satisfied

Figure 15 shows eigenvalues of singlets (blue lines) and triplets (red lines) as a function of  $\Delta$  for  $\hbar\omega_0 = 7.28$  meV and  $x_0 = 50$  nm with (a)  $\epsilon = 0$ , (b)  $\epsilon = 3.2$  meV, (c)  $\epsilon = 3.4$  meV and (d)  $\epsilon = 3.6$  meV.

## Appendix D: Nearest-neighbor exchange energy $J_{nn}$

### 1. Two electrons in a DQD device

#### a. Effective Hamiltonian

A two-electron system in a DQD device can be analyzed by discarding the right-most dot in a TQD device, cf. Fig. 16, and redefine the DQD potential as

$$V_{\text{DQD}}(\mathbf{r}) = \frac{1}{2} m \omega_0^2 \left( \text{Min} \left[ \left( x + \frac{x_0}{2} \right)^2, \left( x - \frac{x_0}{2} \right)^2 + \Delta \right] + y^2 \right), \quad (\text{D1})$$

such that  $h_j = (-i\hbar\nabla_j + e\mathbf{A}/c)^2/2m^* + V_{\text{DQD}}(\mathbf{r}) + g^* \mu_B \mathbf{B} \cdot \mathbf{S}$ .

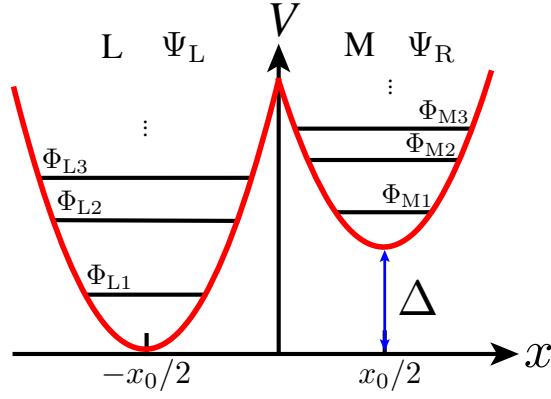


FIG. 16: Schematic illustration of the potential function in a DQD device with inter-dot distance  $x_0$ . The orthonormalized F-D states in left (L) (right (R)) dot are labeled as  $\Phi_{L_j}$  ( $\Phi_{R_j}$ ) for ground ( $j = 1$ ) and  $(j - 1)$ -th excited orbitals. The wavefunctions in dot L and R which give the converged value of  $J_{\text{nn(DQD)}}$  are denoted as  $\Psi_L$  and  $\Psi_R$  respectively.

For a singlet-triplet qubit defined in the regime where each dot is singly occupied [75], the qubit parameters are the nearest-neighbor (nn) exchange energy  $J_{\text{nn(DQD)}}$  and magnetic gradient across two dots  $\delta B$ . Practically, in single-qubit operations, only  $J_{\text{nn(DQD)}}$  is electrically tuned while  $\delta B$  maintains constant.  $J_{\text{nn(DQD)}}$  is defined by the energy splitting between lowest singlet and triplet state, i.e.  $J_{\text{nn(DQD)}} = E_{|T(11)\rangle} - E_{|S(11)\rangle}$ . When the applied external magnetic field  $B$  is not sufficiently large to induce negative singlet-triplet splitting in a doubly occupied quantum-dot (QD) [68, 69], i.e.  $E_{|T(02)\rangle} - E_{|S(02)\rangle} < 0$ ,  $J_{\text{nn(DQD)}}$  is generally conceived to be positive at  $\Delta = 0$  [76, 77] and increases monotonically as a function of detuning  $\Delta$ , as demonstrated in most experiments [3, 21, 78–82]. Using the generic Hubbard Model (see Appendix B), the Hamiltonian written in the bases of  $|S(11)\rangle$ ,  $|S(20)\rangle$ ,  $|S(02)\rangle$  and  $|T(11)\rangle$  is

$$H = \begin{pmatrix} J_{L,M}^e + U'_{L,M} + \Delta & \sqrt{2}t'_{L,M} & \sqrt{2}t'_{L,M} & 0 \\ \sqrt{2}t'_{L,M} & U_L & J_{L,M}^p & 0 \\ \sqrt{2}t'_{L,M} & J_{L,M}^p & U_L + 2\Delta & 0 \\ 0 & 0 & 0 & -J_{L,M}^e + U'_{L,M} + \Delta \end{pmatrix}, \quad (\text{D2})$$

where  $J_{L,M}^j = J_{L(L,M)}^t + t_{L,M}$  and dot L and R are considered to be symmetric. Taking the Schrieffer-Wolff (S-W) transformation [66, 67, 83], we have

$$\begin{aligned} J_{\text{nn(DQD)}} &= E_{|T(11)\rangle} - E_{|S(11)\rangle} \\ &\approx \left[ \sum_{s=0}^1 \frac{(\sqrt{2}t'_{L,M})^2}{U_L - U'_{L,M} - J_{L,M}^e + (-1)^s \Delta} \right] - 2J_{L,M}^e \\ &= J_{\text{nn(DQD)}}^t - 2J_{L,M}^e, \end{aligned} \quad (\text{D3})$$

where  $J_{\text{nn(DQD)}}^t$  is the inter-dot tunneling contribution to  $J_{\text{nn(DQD)}}$  while “(DQD)” is included explicitly in the subscript to signify its slight difference compared to the TQD case which we will discuss in Appendix D 2. Note that Eq. (D3) is equivalent to Hund-Mulliken (H-M) approximation [67, 84, 85].

#### b. Values of $J_{\text{nn(DQD)}}$ and CI calculation

$\Psi_j$  in Eq. (B2) refers to the wavefunctions which give converged values of  $J_{\text{nn(DQD)}}$ . In Eq. (D3), the term  $J_{\text{nn(DQD)}}^t$  arises due to the admixture between the singlets while  $-2J^e$  term is the energy splitting between  $|S(11)\rangle$  and  $|T(11)\rangle$ . When the excited orbitals ( $\Phi_{\lambda_j}$  for  $j > 1$  and  $\lambda \in \{L,R\}$ ) exhibit non-negligible effect on  $J_{\text{nn(DQD)}}$ ,  $\Psi_{\lambda_j} \neq \Phi_{\lambda_j}$ , hence full CI calculations are required to obtain an accurate  $J_{\text{nn(DQD)}}$ . On the other hand, for the case in which the effects of excited orbitals can be neglected, i.e.  $\Psi_{\lambda_j} = \Phi_{\lambda_j}$ , e.g. Heitler-London (H-L) or Hund-Mulliken (H-M) approximation [67, 84, 85]. In this case, together with the condition  $B = 0$ ,  $J_{L,M}^e > 0$  as suggested by Eq. (B2d),

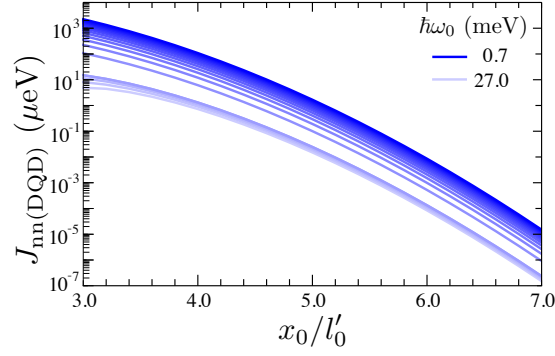


FIG. 17: Nearest-neighbour exchange energy  $J_{\text{nn(DQD)}}$  v.s. inter-dot distance  $x_0$ .  $x_0$  is presented as a ratio to the Fock-Darwin radius,  $l'_0 = \sqrt{\hbar/m^* \omega_0}$ . The lightness of the color for the solid lines indicates the confinement strength  $\hbar\omega_0$ . The magnetic field for each set of parameters are chosen such that  $\hbar\omega_c = 2/\sqrt{99} \times \hbar\omega_0$ .

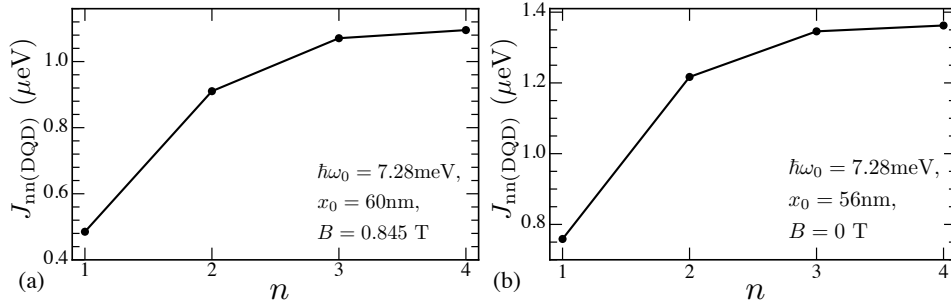


FIG. 18: Nearest-neighbor exchange energy  $J_{\text{nn(DQD)}}$  of two-electron state in an un-detuned DQD ( $\Delta = 0$ ). The horizontal axis indicates the number of orbitals retained in the CI calculation, where the principle quantum number  $n = 1$  ( $2, 3, 4$ ) corresponds to  $6$  ( $12, 20, 30$ ) orbitals.  $J_{\text{nn(DQD)}}$  is evaluated for (a)  $B = 0.845$  T and (b)  $B = 0$ , as indicated in the lower right corner of each subfigure.

since  $\Phi_{L1}^*(\mathbf{r}_j)\Phi_{M1}(\mathbf{r}_j)$ ,  $\Phi_{M1}^*(\mathbf{r}_j)\Phi_{L1}(\mathbf{r}_j)$  and  $e^2/\epsilon|\mathbf{r}_1 - \mathbf{r}_2|$  are positive for any value of  $\mathbf{r}_j$ .

If  $J_{\text{nn(DQD)}}^t > 2J_{L,M}^e$ ,  $J_{\text{nn(DQD)}} > 0$ . On the other hand, if  $J_{\text{nn(DQD)}}^t < 2J_{L,M}^e$ ,  $J_{\text{nn(DQD)}} < 0$ . The former case is observed in experiments whenever a weak magnetic field strength is applied [3, 78–82, 86]. The later case is never observed in experiments for weak magnetic field strengths.

Figure 17 shows  $J_{\text{nn(DQD)}}$  evaluated using Eq. (D3) and Eq. (B2) by assuming  $\Psi_{\eta j} = \Phi_{\eta j}$  (H-M approximation) [67, 84, 85]. Fig. 17 shows that for a large range of parameters considered,  $J_{\text{nn(DQD)}} > 0$ , indicating that  $J_{\text{nn(DQD)}}$  is dominated by the tunneling induced term  $J_{\text{nn(DQD)}}^t$  in most cases.

We extend the discussion of  $J_{\text{nn(DQD)}}$  by going into the regime of full CI calculations in which accurate  $J_{\text{nn(DQD)}}$  can be determined by increasing the number of orthogonalized F-D states in the calculations until the results converge. Fig. 18 shows two examples of  $J_{\text{nn(DQD)}}$  evaluated at  $B > 0$  (cf. Fig. 18(a)) and  $B = 0$  (cf. Fig. 18(b)), which show  $J_{\text{nn(DQD)}}$  converges at  $n = 3$ . In particular,  $J_{\text{nn(DQD)}}$  yields 2.30% (1.23%) change in magnitude when the orbitals retained in the CI calculation increases from  $n = 3$  to  $n = 4$  for  $B > 0$  ( $B = 0$ ). From full CI results, the lowest singlet and triplet eigenstate, denoted as  $|S(11)'\rangle$  and  $|T(11)'\rangle$  respectively, can be expanded as

$$\begin{aligned} |S(11)'\rangle &= \sum c_{k,l}^S |\widetilde{S(11)}\rangle_{k,l} + c_{m,n}^S |\widetilde{S(02)}\rangle_{m,n} + c_{o,p}^S |\widetilde{S(20)}\rangle_{o,p}, \\ |T(11)'\rangle &= \sum c_{k,l}^T |\widetilde{T(11)}\rangle_{k,l} + c_{m,n}^T |\widetilde{T(02)}\rangle_{m,n} + c_{o,p}^T |\widetilde{T(20)}\rangle_{o,p}, \end{aligned} \quad (\text{D4})$$

see Eq. (B9) for the definition of two-electron Slater determinants  $|\widetilde{\eta}\rangle$ . Due to the normalization conditions, we have

$$\begin{aligned} \sum |c_{k,l}^S|^2 + |c_{m,n}^S|^2 + |c_{o,p}^S|^2 &= 1, \\ \sum |c_{k,l}^T|^2 + |c_{m,n}^T|^2 + |c_{o,p}^T|^2 &= 1. \end{aligned} \quad (\text{D5})$$



Parameters	$J_{\text{nn(DQD)}} (\mu\text{eV})$	$E_{ T(11)\rangle} - E_{ S(11)\rangle} = -2J_{\text{L,M}}^e (\mu\text{eV})$
$x_0 = 60\text{nm}, B = 0.845 \text{ T}$	0.274	-0.198
$x_0 = 56\text{nm}, B = 0$	1.362	-0.959

TABLE I: Nearest-neighbor exchange energy,  $J_{\text{nn(DQD)}}$ , of two-electron states in an un-detuned DQD device ( $\Delta = 0$ ). The corresponding singlet-triplet splitting of raw  $|S(11)\rangle$  and  $|T(11)\rangle$ , i.e.  $E_{|T(11)\rangle} - E_{|S(11)\rangle}$ , is shown. The values are obtained for  $n = 4$  (cf. Fig. 18).

We can obtain the eigenvalues of  $|S(11)\rangle$  and  $|T(11)\rangle$  from full CI results by taking

$$\begin{aligned}
E_{|S(11)\rangle} &= \left( \frac{1}{\sum_{k,k',l,l'} (c_{k',l'}^S)^* c_{k,l}^S} \right) \times \sum_{k,k',l,l'} \left[ (c_{k',l'}^S)^* c_{k,l}^S (|\widetilde{S(11)}\rangle_{k',l'})^\dagger \left( \sum_j h_j + H_C \right) |\widetilde{S(11)}\rangle_{k,l} \right], \\
E_{|T(11)\rangle} &= \left( \frac{1}{\sum_{k,k',l,l'} (c_{k',l'}^T)^* c_{k,l}^T} \right) \times \sum_{k,k',l,l'} \left[ (c_{k',l'}^T)^* c_{k,l}^T (|\widetilde{T(11)}\rangle_{k',l'})^\dagger \left( \sum_j h_j + H_C \right) |\widetilde{T(11)}\rangle_{k,l} \right],
\end{aligned} \tag{D6}$$

where the asterisk indicates complex conjugate.

Table I provides the values obtained using Eq. (D6) with the corresponding  $J_{\text{nn(DQD)}} = E_{|T(11)\rangle} - E_{|S(11)\rangle}$ . The results show that  $E_{|T(11)\rangle} - E_{|S(11)\rangle} = -2J^e < 0$  for a converged positive  $J_{\text{nn(DQD)}}$  (cf. Eq. (D3)). This demonstrates that the Coulomb exchange terms,  $J_{j,k}^e$  can always be conceived to yield positive values.

## 2. Two electrons in a TQD device

Nearest-neighbor exchange  $J_{\text{nn}}$  in a TQD device materializes when the two-electron states are coupled through nearest-neighbor tunneling. Note that  $J_{\text{nn}}$  gives rise to exchange energy *indirectly* in a TQD device in (101) region (see Appendix F for details), in contrast to the case in which  $J_{\text{nn(DQD)}}$  *directly* yields the exchange energy in a DQD device in (11) region. In this work, we consider  $J_{\text{nn}}$  in two situations: (1)  $\Delta > 0$ ,  $\varepsilon = 0$  and (2)  $\Delta > 0$ ,  $\varepsilon > 0$ , see Fig. 1 for the definition of detunings. Also, we consider all three dots to be symmetric, i.e. having the same values of  $\hbar\omega_0$ .

### a. $\Delta > 0$ , $\varepsilon = 0$

When  $\varepsilon = 0$  and  $\Delta > 0$ , the lowest energy subspace is spanned by  $|S(101)\rangle$ ,  $|T(101)\rangle$ ,  $|S(110)\rangle$ ,  $|S(011)\rangle$ ,  $|T(110)\rangle$ ,  $|T(011)\rangle$ ,  $|S(002)\rangle$ ,  $|S(200)\rangle$  and  $|S(020)\rangle$ , cf. Fig. 3(c)-(d), Fig. 3(i)-(j) and Fig. 10. The hybridized bases giving rise to  $J_{\text{nn}}$  are  $|S(110; 011)^+\rangle$ ,  $|S(200; 002)^+\rangle$ ,  $|S(020)\rangle$  and  $|T(110; 011)^-\rangle$ , where

$$\begin{aligned}
|S(110; 011)^+\rangle &= \frac{1}{2} (|S(110)\rangle + |S(011)\rangle), \\
|S(200; 002)^+\rangle &= \frac{1}{2} (|S(200)\rangle + |S(002)\rangle), \\
|T(110; 011)^-\rangle &= \frac{1}{2} (|T(110)\rangle - |T(011)\rangle),
\end{aligned} \tag{D7}$$

while the decoupled states with similar energies are  $|S(110; 011)^-\rangle$  and  $|T(110; 011)^+\rangle$ , defined as

$$\begin{aligned}
|S(110; 011)^-\rangle &= \frac{1}{2} (|S(110)\rangle - |S(011)\rangle), \\
|T(110; 011)^+\rangle &= \frac{1}{2} (|T(110)\rangle + |T(011)\rangle).
\end{aligned} \tag{D8}$$

Since energies of  $|T(200)\rangle$ ,  $|T(002)\rangle$ ,  $|T(020)\rangle$  yield much larger values, they are neglected, cf. Fig. 3(c)-(d) and Fig. 3(i)-(j). Since  $E_{|S(110)\rangle} = E_{|S(011)\rangle}$ ,  $E_{|T(110)\rangle} = E_{|T(011)\rangle}$  and  $E_{|S(200)\rangle} = E_{|S(002)\rangle}$ , they form hybridized states. Using the generic Hubbard Model (see Appendix B), the Hamiltonian written in the bases of  $|S(110; 011)^+\rangle$ ,  $|S(020)\rangle$ ,

$|S(200;002)^+\rangle$  and  $|T(110;011)^-\rangle$  is

$$H = \begin{pmatrix} U'_{L,M} + (J_{L,M}^e + t''_{L,R}) + \Delta & 2t'_{L,M} & \sqrt{2}t'_{L,M} & 0 \\ 2t'_{L,M} & U_L + 2\Delta & \sqrt{2}J_{L,M}^p & 0 \\ \sqrt{2}t'_{L,M} & \sqrt{2}J_{L,M}^p & J_{L,R}^p + U_L & 0 \\ 0 & 0 & 0 & U'_{L,M} - (J_{L,M}^e + t''_{L,R}) + \Delta \end{pmatrix}, \quad (\text{D9})$$

where  $t'_{L,M} = t_{L,M} + J_{L(L,M)}^t = t_{L,M} + J_{M(L,M)}^t$ ,  $t'_{L,R} = J_{L(L,R)}^t + t_{L,R}$ ,  $t''_{L,R} = t_{L,R} + J_{M(L,R)}^t$ . Performing S-W transformation on the subspace spanned by the singlets, we obtain the eigenvalue of the ground singlet

$$E_{|S(110)^+\rangle} = E_{|S(110)^+\rangle} - \frac{1}{2} \frac{2(2t'_{L,M})^2}{U_L - U'_{L,M} - (J_{L,M}^e + t''_{L,R}) + \Delta} - \frac{1}{2} \frac{2(\sqrt{2}t'_{L,M})^2}{U_L - U'_{L,M} - (J_{L,M}^e + t''_{L,R}) + J_{L,R}^p - \Delta}. \quad (\text{D10})$$

The S-W transformation is equivalent to applying a unitary transformation  $U$  on  $H$  (Eq. (D9)), i.e.  $U^\dagger H U$ , with

$$U = \begin{pmatrix} 1 - \frac{1}{8} \tan^2 \theta_{|S(020)\rangle} - \frac{1}{8} \tan^2 \theta_{|S(200;002)^+\rangle} & \frac{1}{2} \tan \theta_{|S(020)\rangle} & \frac{1}{2} \tan \theta_{|S(200;002)^+\rangle} \\ -\frac{1}{2} \tan \theta_{|S(020)\rangle} & 1 - \frac{1}{8} \tan^2 \theta_{|S(020)\rangle} & -\frac{1}{8} \tan \theta_{|S(020)\rangle} \tan \theta_{|S(200;002)^+\rangle} \\ \frac{1}{2} \tan \theta_{|S(200;002)^+\rangle} & -\frac{1}{8} \tan \theta_{|S(020)\rangle} \tan \theta_{|S(200;002)^+\rangle} & 1 - \frac{1}{8} \tan^2 \theta_{|S(200;002)^+\rangle} \end{pmatrix}, \quad (\text{D11})$$

where  $\theta_{|S(020)\rangle}$  ( $\theta_{|S(200;002)^+\rangle}$ ) is the admixture angle between  $|S(110;011)^+\rangle$  and  $|S(020)\rangle$  ( $|S(200;002)^+\rangle$ ), defined as

$$\begin{aligned} \tan \theta_{|S(020)\rangle} &= \frac{4t'_{L,M}}{E_{|S(020)\rangle} - E_{|S(110;011)^+\rangle}} \\ &= \frac{4t'_{L,M}}{U_L - U'_{L,M} - (J_{L,M}^e + t''_{L,R}) + \Delta}, \end{aligned} \quad (\text{D12a})$$

$$\begin{aligned} \tan \theta_{|S(200;002)^+\rangle} &= \frac{2\sqrt{2}t'_{L,M}}{E_{|S(200;002)^+\rangle} - E_{|S(110;011)^+\rangle}} \\ &= \frac{2\sqrt{2}t'_{L,M}}{U_L - U'_{L,M} - (J_{L,M}^e + t''_{L,R}) + J_{L,R}^p - \Delta}. \end{aligned} \quad (\text{D12b})$$

From Eq. (D9) and Eq. (D10), the nearest-neighbor exchange is

$$J_{\text{nn}}(\Delta, \varepsilon = 0) = \left[ \frac{(2t'_{L,M})^2}{E_{|S(020)\rangle} - E_{|S(110;011)^+\rangle}} + \frac{(\sqrt{2}t'_{L,M})^2}{E_{|S(200;002)^+\rangle} - E_{|S(110;011)^+\rangle}} - (2J_{L,M}^e + t''_{L,R}) \right] \quad (\text{D13a})$$

$$\begin{aligned} &= \left[ \frac{(2t'_{L,M})^2}{U_L - U'_{L,M} - (J_{L,M}^e + t''_{L,R}) + \Delta} + \frac{(\sqrt{2}t'_{L,M})^2}{U_L - U'_{L,M} - (J_{L,M}^e + t''_{L,R}) + J_{L,R}^p - \Delta} \right] \\ &\quad - (2J_{L,M}^e + t''_{L,R}) \end{aligned} \quad (\text{D13b})$$

$$\approx \left[ \frac{(2t'_{L,M})^2}{U_L - U'_{L,M} - J_{L,M}^e + \Delta} + \frac{(\sqrt{2}t'_{L,M})^2}{U_L - U'_{L,M} - J_{L,M}^e - \Delta} \right] - 2J_{L,M}^e \quad (\text{D13c})$$

$$= 2(t'_{L,M})^2 [2\xi_{\text{nn}}^{|S(020)\rangle} + \xi_{\text{nn}}^{|S(200;002)^+\rangle}] - 2J_{L,M}^e \quad (\text{D13d})$$

$$= 2(t'_{L,M})^2 \xi_{\text{nn}}(\Delta, \varepsilon = 0) - 2J_{L,M}^e \quad (\text{D13e})$$

$$= J_{\text{nn}}^t(\Delta, \varepsilon = 0) - 2J_{L,M}^e \quad (\text{D13f})$$

where we define the nearest-neighbor tunneling contribution to the  $J_{\text{nn}}$  as  $J_{\text{nn}}^t$  with

$$J_{\text{nn}}^t(\Delta, \varepsilon = 0) = 2 (t'_{\text{L,M}})^2 \xi_{\text{nn}}(\Delta, \varepsilon = 0). \quad (\text{D14})$$

Eq. (D13c) is obtained from Eq. (D13b) by recognizing that, compared to other terms in the expression, terms involving tunneling between outmost dots are negligible. Also, we introduce the notation  $\xi_{\text{nn}}^\eta$  to denote the effect on  $J_{\text{nn}}^t$  by the admixture between  $|S(110;011)^+\rangle$  and  $|\eta\rangle$ , where

$$\begin{aligned} \xi_{\text{nn}}^{|S(200;002)^+\rangle} &= \frac{1}{E_{|S(200;002)^+\rangle} - E_{|S(110;011)^+\rangle}} = \frac{1}{U_{\text{L}} - U'_{\text{L,M}} - J_{\text{L,M}}^e - \Delta}, \\ \xi_{\text{nn}}^{|S(020)\rangle} &= \frac{1}{E_{|S(020)\rangle} - E_{|S(110;011)^+\rangle}} = \frac{1}{U_{\text{L}} - U'_{\text{L,M}} - J_{\text{L,M}}^e + \Delta}. \end{aligned} \quad (\text{D15})$$

$J_{\text{nn}}$ ,  $J_{\text{nn}}^t$  and  $\xi_{\text{nn}}$  are written as functions of  $\Delta$  and  $\varepsilon$  with  $\varepsilon = 0$  to distinguish them from those with  $\varepsilon > 0$ , which will be discussed in Appendix D2b. In general, the limits in which  $U_{\text{L}} - U'_{\text{L,M}} + \Delta - J_{\text{L,M}}^e \gg t''_{\text{L,R}}$  and  $U_{\text{L}} - U'_{\text{L,M}} - J_{\text{L,M}}^e \gg t''_{\text{L,R}} - J_{\text{L,R}}^p$  apply, which lead to Eq. (D13) being the same form as  $J_{\text{nn(DQD)}}$  (Eq. (D3)), except for the term containing  $(+\Delta)$  yields a larger numerator by a factor of 2.

*b.  $\Delta > 0, \varepsilon > 0, E_{|S(002)\rangle} > E_{|S(011)\rangle} > E_{|S(101)\rangle}$  in (101) region*

When  $\varepsilon > 0$ , we consider the regime where  $E_{|S(002)\rangle} > E_{|S(011)\rangle}$  and  $E_{|S(020)\rangle} > E_{|S(011)\rangle}$ , cf. Fig. 12 and 13. Also, the hybridized states, e.g.  $|S(110);011\rangle^\pm$ , are absent due to the non-zero  $\varepsilon$ , i.e.  $2\varepsilon = E_{|S(110)\rangle} - E_{|S(011)\rangle} = E_{|T(110)\rangle} - E_{|T(011)\rangle} = (E_{|S(200)\rangle} - E_{|S(002)\rangle})/2 > 0$ . Using the generic Hubbard Model (see Appendix B), the Hamiltonian written in the bases of  $|S(011)\rangle, |S(002)\rangle, |S(020)\rangle$  and  $|T(011)\rangle$  is

$$H = \begin{pmatrix} U'_{\text{L,M}} + J_{\text{L,M}}^e + \Delta - \varepsilon & \sqrt{2}t'_{\text{L,M}} & \sqrt{2}t'_{\text{L,M}} & 0 \\ \sqrt{2}t'_{\text{L,M}} & U_{\text{L}} - 2\varepsilon & J_{\text{L,M}}^p & 0 \\ \sqrt{2}t'_{\text{L,M}} & J_{\text{L,M}}^p & U_{\text{L}} + 2\Delta & 0 \\ 0 & 0 & 0 & U'_{\text{L,M}} - J_{\text{L,M}}^e + \Delta - \varepsilon \end{pmatrix}. \quad (\text{D16})$$

Following the same procedures from Eq. (D10) to (D13), we have

$$J_{\text{nn}}(\Delta, \varepsilon > 0) = \frac{2 (t'_{\text{L,M}})^2}{E_{|S(002)\rangle} - E_{|S(011)\rangle}} + \frac{2 (t'_{\text{L,M}})^2}{E_{|S(020)\rangle} - E_{|S(011)\rangle}} - 2J_{\text{L,M}}^e \quad (\text{D17a})$$

$$\approx \frac{2 (t'_{\text{L,M}})^2}{E_{|S(002)\rangle} - E_{|S(011)\rangle}} - 2J_{\text{L,M}}^e \quad (\text{D17b})$$

$$= \frac{2 (t'_{\text{L,M}})^2}{U_{\text{L}} - U'_{\text{L,M}} - J_{\text{L,M}}^e - (\Delta + \varepsilon)} - 2J_{\text{L,M}}^e \quad (\text{D17c})$$

$$= 2 (t'_{\text{L,M}})^2 \xi_{\text{nn}}^{|S(020)\rangle} - 2J_{\text{L,M}}^e \quad (\text{D17d})$$

$$= 2 (t'_{\text{L,M}})^2 \xi_{\text{nn}}(\Delta, \varepsilon > 0) - 2J_{\text{L,M}}^e \quad (\text{D17e})$$

$$= J_{\text{nn}}^t(\Delta, \varepsilon > 0) - 2J_{\text{L,M}}^e, \quad (\text{D17f})$$

where the identities of  $\xi_{\text{nn}}^{|\eta\rangle}$  and  $\xi_{\text{nn}}$  are similar to Eq. (D15). Eq. (D17b) is obtained from Eq. (D17a) by recognizing that  $E_{|S(020)\rangle} - E_{|S(011)\rangle} \gg E_{|S(002)\rangle} - E_{|S(011)\rangle}$ , cf. Fig. 12 and Fig. 13.

### Appendix E: Prove the likelihood of $J_{\text{L,R}}^t \ll 2J_{\text{L,R}}^e$ at $\varepsilon = 0$ for large $x_0$

In this section, we show that for a two-electron system in a TQD device in (101) region, it is most likely for  $J_{\text{L,R}}^t \ll 2J_{\text{L,R}}^e$  to occur at large  $x_0$ . Following Eq. (D3), we have for the *direct* long-range exchange

$$J_{L,R} \approx J_{L,R}^t - 2J_{L,R}^e, \quad (\text{E1})$$

where

$$J_{L,R}^t = \frac{4t_{L,R}^2}{U_L - U'_{L,R} - J_{L,R}^e} \quad (\text{E2})$$

Full CI calculations in Appendix D 1 b reveals that  $\langle S(02)|S(11) \rangle = \langle S(20)|S(11) \rangle = t'_{L,M} = t_{L,M} + J_{L(L,M)}^t < 0$ . Since  $J_{L(L,M)}^t > 0$ , it is reasonable to perceive  $t'_{L,M}$  is dominated by  $t_{L,M}$ . The inclusion of  $J_{L(L,M)}^t$  in  $t'_{L,M}$  leads to reduction of the magnitude  $|t'_{L,M}|$ . Hence, in Eq. (E2), we have dropped the term  $J_{L(L,R)}^t$  in  $t'_{L,R}$ , s.t.  $t'_{L,R} \approx t_{L,R}$ , to maximize the effect of  $J_{L,R}^t$  in  $J_{L,R}$ . Assuming the values of  $t_{L,M}$  and  $J_{L,M}^e$  obtained using F-D states can qualitatively describe the accurate results, we have

$$t_{L,R} = \int \Phi_{L1}(\mathbf{r}) h \Phi_{R1}(\mathbf{r}) \quad (\text{E3a})$$

$$= -\hbar\omega_0 e^{-\tilde{x}_0^2} \left( \frac{1}{\sqrt{\pi}} \tilde{x}_0 - 1 \right),$$

$$\approx -\hbar\omega_0 e^{-\tilde{x}_0^2} \left( \frac{1}{\sqrt{\pi}} \tilde{x}_0 \right),$$

$$J_{L,R}^e = \int \Phi_{L1}(\mathbf{r}_1) \Phi_{R1}(\mathbf{r}_2) H_C \Phi_{R1}(\mathbf{r}_1) \Phi_{L1}(\mathbf{r}_2) \quad (\text{E3b})$$

$$= \frac{e^2 \sqrt{\pi}}{l_0 \epsilon \sqrt{2}} e^{-\tilde{x}_0^2},$$

where  $l_0 = \sqrt{\hbar/m^* \omega_0}$ ,  $\tilde{x}_0 = x_0/l_0$  and  $B = 0$ . We obtain the third line of Eq. (E3a) since we are considering large  $x_0$  limit,  $\tilde{x}_0 = x_0/l_0 \gg 1$ . We take the ratio

$$\frac{t_{L,R}^2}{J_{L,R}^e} \approx \left( \frac{\hbar^2 \omega^2 l_0 \epsilon \sqrt{2}}{e^2 \pi \sqrt{\pi}} \right) \tilde{x}_0^2 e^{-\tilde{x}_0^2}, \quad (\text{E4})$$

whose derivative with respect to  $\tilde{x}_0$  is

$$\frac{\partial}{\partial \tilde{x}_0} \left( \frac{t_{L,R}^2}{J_{L,R}^e} \right) \propto \tilde{x}_0 (1 - \tilde{x}_0^2) e^{-\tilde{x}_0^2} < 1 \quad (\text{E5})$$

The derivative (Eq. (E5)) yields negative values since  $\tilde{x}_0 > 1$  for any multi-quantum-dot devices, indicating that the reduction of  $t_{L,R}^2$  is more significant than  $J_{L,R}^e$  when  $x_0$  increases in large  $x_0$  regime. Also, since larger  $x_0$  gives smaller  $U'_{L,R}$ , the value of  $J_{L,R}^t$  is further reduced due to the larger denominator. These lead to the reduction of  $J_{L,R}^t$  to be more substantial than  $J_{L,R}^e$ . Therefore, when  $x_0$  is large, it is expected that  $J_{L,R}^t \ll 2J_{L,R}^e$ , such that  $J_{L,R} \approx -2J_{L,R}^e$ .

## Appendix F: Superexchange energy $J_{se}$ for two electrons in a TQD device

### 1. $\Delta > 0$ , $\varepsilon = 0$ , $E_{|S(002)\rangle} > E_{|S(011)\rangle}$ in (101) region

We consider the regime where  $\varepsilon = 0$  and  $\Delta > 0$ . In that regime, the bases in the lowest energy subspace, ordered from the lowest to highest energy, are  $|S(101)\rangle$ ,  $|S(110; 011)^\pm\rangle$ ,  $|S(200; 002)^\pm\rangle$ ,  $|S(020)\rangle$  for singlets and  $|T(101)\rangle$ ,  $|T(110; 011)^\pm\rangle$  for triplets (see Fig. 3(c)-(d) and Fig. 3(i)-(j) for reference). Written in the bases of lowest two singlets,  $|S(101)\rangle$ ,  $|S(110; 011)^+\rangle$ , and triplets,  $|T(101)\rangle$ ,  $|T(110; 011)^-\rangle$ , the Hamiltonian blocks are

$$H_S = \begin{pmatrix} J_{L,R}^e + U'_{L,R} & \sqrt{2}t'_{L,M} \\ \sqrt{2}t'_{L,M} & [U'_{L,M} + \Delta] + [J_{L,M}^e + t'_{L,R}] - J_{\text{nn}}^t(\Delta, \varepsilon = 0) \end{pmatrix}, \quad (\text{F1a})$$

$$H_T = \begin{pmatrix} -J_{L,R}^e + U'_{L,R} & \sqrt{2}t'_{L,M} \\ \sqrt{2}t'_{L,M} & [U'_{L,M} + \Delta] - [J_{L,M}^e + t'_{L,R}] \end{pmatrix}, \quad (\text{F1b})$$

respectively. An additional term  $J_{\text{nn}}^t$  is included by taking into account the nearest-neighbor exchange interaction  $J_{\text{nn}}$ , as discussed in Appendix D 2 a. Also, as discussed in Appendix E, regarding the energies of  $|S(101)\rangle$  and  $|T(101)\rangle$ , long-range Coulomb exchange term  $J_{L,R}^e$  is retained while the tunneling part  $t_{L,R}$  of the *direct* exchange  $J_{L,R}$  between two outmost dots is dropped.

Denoting the lowest eigenvalue of  $H_S$  and  $H_T$  as  $E_{|S(101)\rangle'}$  and  $E_{|T(101)\rangle'}$  respectively, the superexchange energy is defined as  $J_{\text{se}} = E_{|T(101)\rangle'} - E_{|S(101)\rangle'}$ . From Eq. (F1), we have

$$J_{\text{se}}(\Delta, \varepsilon = 0) \approx \frac{(\sqrt{2}t'_{L,M})^2}{E_{|S(110;011)+} - E_{|S(101)\rangle}} - \frac{(\sqrt{2}t'_{L,M})^2}{E_{|T(110;011)-} - E_{|T(101)\rangle}} - 2J_{L,R}^e$$

$$= \frac{(\sqrt{2}t'_{L,M})^2}{\left( U'_{L,M} - U'_{L,R} + \Delta \right) + \left[ (t'_{L,R} + J_{L,M}^e - J_{L,R}^e) - J_{\text{nn}}^t(\Delta, \varepsilon = 0) \right]} \quad (\text{F2a})$$

$$= \frac{(\sqrt{2}t'_{L,M})^2}{\left( U'_{L,M} - U'_{L,R} + \Delta \right) - (t'_{L,R} + J_{L,M}^e - J_{L,R}^e)} - 2J_{L,R}^e$$

$$\approx \left( \frac{\sqrt{2}t'_{L,M}}{U'_{L,M} - U'_{L,R} + \Delta} \right)^2 \left[ J_{\text{nn}}^t(\Delta, \varepsilon = 0) - 2(t'_{L,R} + J_{L,M}^e - J_{L,R}^e) \right] - 2J_{L,R}^e \quad (\text{F2b})$$

$$\approx \left( \frac{\sqrt{2}t'_{L,M}}{U'_{L,M} - U'_{L,R} + \Delta} \right)^2 \left[ J_{\text{nn}}^t(\Delta, \varepsilon = 0) - 2J_{L,M}^e \right] - 2J_{L,R}^e \quad (\text{F2c})$$

$$\approx \left( \sqrt{2}t'_{L,M} \right)^2 \xi_{\text{se}}(\Delta, \varepsilon = 0) \left[ J_{\text{nn}}^t(\Delta, \varepsilon = 0) - 2J_{L,M}^e \right] - 2J_{L,R}^e \quad (\text{F2d})$$

$$= \hat{J}_{\text{se}(L,M)}^t(\Delta, \varepsilon = 0) \left[ J_{\text{nn}}^t(\Delta, \varepsilon = 0) - 2J_{L,M}^e \right] - 2J_{L,R}^e \quad (\text{F2e})$$

$$= \hat{J}_{\text{se}(L,M)}^t(\Delta, \varepsilon = 0) \times J_{\text{nn}}(\Delta, \varepsilon = 0) - 2J_{L,R}^e, \quad (\text{F2f})$$

where we denote higher-order tunneling term contribution to  $J_{\text{se}}$  as  $\hat{J}_{\text{se}(L,M)}^t(\Delta, \varepsilon = 0)$  with

$$\hat{J}_{\text{se}(L,M)}^t(\Delta, \varepsilon = 0) \approx \left( \frac{\sqrt{2}t'_{L,M}}{E_{|S(110;011)+} - E_{|S(101)\rangle}} \right)^2$$

$$= \left( \sqrt{2}t'_{L,M} \right)^2 \left( \frac{1}{U'_{L,M} - U'_{L,R} + \Delta} \right)^2 \quad (\text{F3})$$

$$= \left( \sqrt{2}t'_{L,M} \right)^2 \xi_{\text{se}}(\Delta, \varepsilon = 0).$$

with  $\xi_{\text{se}}$  indicating the effect of  $E_{|S(110;011)+} - E_{|S(101)\rangle}$  and  $E_{|T(110;011)-} - E_{|T(101)\rangle}$  on  $\hat{J}_{\text{se}}^t$ . Eq. (F2a) is obtained by Taylor expanding  $E_{|S(101)\rangle'}$  and  $E_{|T(101)\rangle'}$  up to  $\mathcal{O} \left[ t'_{L,M} / \left( \sum_{j,k} c_{j,k} U'_{j,k} + \Delta \right) \right]^2$  where  $c_{j,k}$  is the coefficient of the term  $U'_{j,k}$ . The approximation is valid as  $\left[ t'_{L,M} / \left( \sum_{j,k} c_{j,k} U'_{j,k} + \Delta \right) \right] \sim 10^{-2}$ . Eq. (F2b) is obtained by Taylor expanding Eq. (F2a) up to  $\mathcal{O} \left[ \left( t'_{L,R} + \sum_{m,n} c_{m,n} J_{m,n}^e \right) / \left( \sum_{j,k} c_{j,k} U'_{j,k} + \Delta \right) \right]$  as the numerator is in the scale of  $\mu\text{eV}$  while the denominator is in the scale of  $\text{meV}$ . Eq. (F2c) is obtained by dropping the term  $t'_{L,R}$  as it yields much smaller magnitude compared to the nearest-neighbor terms. Eq. (F2c) shows that the tunability of superexchange  $J_{\text{se}}$  is determined by the interplay between nearest-neighbor exchange  $J_{\text{nn}}^t(\Delta, \varepsilon = 0)$ , nearest-neighbor tunneling induced term  $\hat{J}_{\text{se}}^t$  and Coulomb exchange term  $J_{L,R}^e$ . In Eq. (F2f), the notation  $J_{\text{nn}}$  is adopted to represent the term  $J_{\text{nn}}^t - 2J_{L,M}^e$ , in analogy to nearest-neighbor exchange in two-electron system in a DQD device.

**2.  $\Delta > 0, \varepsilon > 0, E_{|S(002)\rangle} > E_{|S(011)\rangle}$  in (101) region**

In the regime where  $\varepsilon > 0$  and  $\Delta > 0$ , the bases in the lowest energy subspace are  $|S(101)\rangle, |S(011)\rangle$  for singlets and  $|T(101)\rangle, |T(011)\rangle$  for triplets, cf. Figs. 12 and 13. Written in the bases above, the Hamiltonian blocks for singlets and triplets are

$$H_S = \begin{pmatrix} J_{L,R}^e + U'_{L,R} & t'_{L,M} \\ t'_{L,M} & (U'_{L,M} + \Delta - \varepsilon) + J_{L,M}^e - J_{\text{nn}}^t(\Delta, \varepsilon > 0) \end{pmatrix}, \quad (\text{F4a})$$

$$H_T = \begin{pmatrix} -J_{L,R}^e + U'_{L,R} & t'_{L,M} \\ t'_{L,M} & (U'_{L,M} + \Delta - \varepsilon) - J_{L,M}^e \end{pmatrix}, \quad (\text{F4b})$$

respectively. An additional term  $J_{\text{nn}}^t$  is included by taking into account the nearest-neighbor exchange interaction  $J_{\text{nn}}$ , as discussed in Appendix D2b. Also, as discussed in Appendix E, regarding the energies of  $|S(101)\rangle$  and  $|T(101)\rangle$ , long-range Coulomb exchange term  $J_{L,R}^e$  is retained while the tunneling part  $t_{L,R}$  of the *direct* exchange  $J_{L,R}$  between two outmost dots is dropped.

Denoting the lowest eigenvalue of  $H_S$  and  $H_T$  as  $E_{|S(101)\rangle'}$  and  $E_{|T(101)\rangle'}$  respectively, the superexchange energy  $J_{\text{se}}$  is defined as  $J = E_{|T(101)\rangle'} - E_{|S(101)\rangle'}$ . From Eq. (F1), we have

$$\begin{aligned} J_{\text{se}}(\Delta, \varepsilon > 0) &\approx \frac{(t'_{L,M})^2}{E_{|S(011)\rangle} - E_{|S(101)\rangle}} - \frac{(t'_{L,M})^2}{E_{|T(011)\rangle} - E_{|T(101)\rangle}} - 2J_{L,R}^e \\ &= \frac{(t'_{L,M})^2}{\left( U'_{L,M} - U'_{L,R} + \Delta - \varepsilon \right) + \left[ \left( J_{L,M}^e - J_{L,R}^e \right) - J_{\text{nn}}^t(\Delta, \varepsilon > 0) \right]} \end{aligned} \quad (\text{F5a})$$

$$\begin{aligned} &- \frac{(t'_{L,M})^2}{\left( U'_{L,M} - U'_{L,R} + \Delta - \varepsilon \right) - \left( J_{L,M}^e - J_{L,R}^e \right)} - 2J_{L,R}^e \\ &\approx \left( \frac{t'_{L,M}}{U'_{L,M} - U'_{L,R} + \Delta - \varepsilon} \right)^2 \left[ J_{\text{nn}}^t(\Delta, \varepsilon > 0) - 2(J_{L,M}^e - J_{L,R}^e) \right] - 2J_{L,R}^e \end{aligned} \quad (\text{F5b})$$

$$\approx \left[ \frac{t'_{L,M}}{U'_{L,M} - U'_{L,R} + (\Delta - \varepsilon)} \right]^2 \left[ J_{\text{nn}}^t(\Delta, \varepsilon > 0) - 2J_{L,M}^e \right] - 2J_{L,R}^e \quad (\text{F5c})$$

$$= (t'_{L,M})^2 \xi_{\text{se}}(\Delta, \varepsilon) \left[ J_{\text{nn}}^t(\Delta, \varepsilon > 0) - 2J_{L,M}^e \right] - 2J_{L,R}^e \quad (\text{F5d})$$

$$= \hat{J}_{\text{se}(L,M)}^t(\Delta, \varepsilon) \left[ J_{\text{nn}}^t(\Delta, \varepsilon > 0) - 2J_{L,M}^e \right] - 2J_{L,R}^e, \quad (\text{F5e})$$

$$= \hat{J}_{\text{se}(L,M)}^t(\Delta, \varepsilon) \times J_{\text{nn}}(\Delta, \varepsilon > 0) - 2J_{L,R}^e, \quad (\text{F5f})$$

$$= \hat{J}_{\text{se}(L,M)}^t(\Delta, \varepsilon) \times J_{\text{nn}}(\Delta, \varepsilon > 0) - 2J_{L,R}^e, \quad (\text{F5g})$$

where we denote higher-order tunneling term contribution to  $J_{\text{se}}$  as  $\hat{J}_{\text{se}(L,M)}^t(\Delta, \varepsilon)$  with

$$\begin{aligned} \hat{J}_{\text{se}(L,M)}^t(\Delta, \varepsilon) &\approx \left( \frac{\sqrt{2}t'_{L,M}}{E_{|S(011)\rangle} - E_{|S(101)\rangle}} \right)^2 \\ &= \left( \sqrt{2}t'_{L,M} \right)^2 \left[ \frac{1}{U'_{L,M} - U'_{L,R} + (\Delta - \varepsilon)} \right]^2 \\ &= \left( \sqrt{2}t'_{L,M} \right)^2 \xi_{\text{se}}(\Delta, \varepsilon > 0). \end{aligned} \quad (\text{F6})$$

$\xi_{\text{se}}$  indicates the effect of  $E_{|S(110)\rangle} - E_{|S(101)\rangle}$  and  $E_{|T(011)\rangle} - E_{|T(101)\rangle}$  on  $\hat{J}_{\text{se}}^t$ . Eq. (F5a) to (F5c) are obtained using Taylor expansion similar to the procedures in Eq. (F2).

**3.  $\Delta > 0, \varepsilon \gg 0, E_{|S(011)\rangle} > E_{|S(002)\rangle}$  in (101) region**

In the regime where  $\Delta > 0$  and  $\varepsilon \gg 0$  such that  $E_{|S(011)\rangle} > E_{|S(002)\rangle}$  in (101) region, the lowest energy bases are  $|S(101)\rangle, |S(002)\rangle, |S(011)\rangle$  for singlets and  $|T(101)\rangle, |T(011)\rangle$  for triplets, cf. Fig. 7(a)-(b) in the main text and Fig. 15 in Appendix C2. The Hamiltonian blocks written in the bases are

$$H_S = \begin{pmatrix} J_{L,R}^e + U'_{L,R} & 0 & t'_{L,M} \\ 0 & U_L - 2\varepsilon & t'_{L,M} \\ t'_{L,M} & t'_{L,M} & J_{L,M}^e + U'_{L,M} + \Delta - \varepsilon \end{pmatrix}, \quad (\text{F7a})$$

$$H_T = \begin{pmatrix} -J_{L,R}^e + U'_{L,R} & t'_{L,M} \\ t'_{L,M} & -J_{L,M}^e + U'_{L,M} + \Delta - \varepsilon \end{pmatrix}. \quad (\text{F7b})$$

$H_S$  is first transformed under a unitary transformation  $U_S^{(1)}$  which diagonalize the subspace spanned by  $|S(002)\rangle$  and  $|S(011)\rangle$

$$\begin{aligned} H_S^{(1)} &= U_S^{(1)\dagger} H_S U_S^{(1)} \\ &= \begin{pmatrix} J_{L,R}^e + U'_{L,R} & t'_{L,M} \sin \frac{\phi_S}{2} & t'_{L,M} \cos \frac{\phi_S}{2} \\ t'_{L,M} \sin \frac{\phi_S}{2} & U_L - 2\varepsilon - \frac{t'_{L,M}}{2} \tan \phi_S & 0 \\ t'_{L,M} \cos \frac{\phi_S}{2} & 0 & J_{L,M}^e + U'_{L,M} + \Delta - \varepsilon + \frac{t'_{L,M}}{2} \tan \phi_S \end{pmatrix}, \end{aligned} \quad (\text{F8})$$

where

$$U_S^{(1)} = \begin{pmatrix} 1 & 0 & 0 \\ 0 & -\cos \frac{\phi_S}{2} & \sin \frac{\phi_S}{2} \\ 0 & \sin \frac{\phi_S}{2} & \cos \frac{\phi_S}{2} \end{pmatrix}^{-1}. \quad (\text{F9})$$

The eigenbases of  $U_S^{(1)\dagger} H_S U_S^{(1)}$  (Eq. (F8)) are

$$\begin{aligned} \overline{|S(101)\rangle} &= |S(101)\rangle, \\ \overline{|S(002)\rangle} &= -\cos \frac{\phi_S}{2} |S(002)\rangle + \sin \frac{\phi_S}{2} |S(011)\rangle, \\ \overline{|S(011)\rangle} &= \sin \frac{\phi_S}{2} |S(002)\rangle + \cos \frac{\phi_S}{2} |S(011)\rangle. \end{aligned} \quad (\text{F10})$$

In Eq. (F9),  $\phi_S$  is the admixture angle between  $|S(002)\rangle$  and  $|S(011)\rangle$  whose expression is

$$\begin{aligned} \tan \phi_S &= \frac{2t'_{L,M}}{E_{|S(011)\rangle} - E_{|S(002)\rangle}} \\ &= \frac{2t'_{L,M}}{\left( J_{L,M}^e + U'_{L,M} + \Delta - \varepsilon \right) - (U_L - 2\varepsilon)}. \end{aligned} \quad (\text{F11})$$

We then adopt S-W transformation up to  $\mathcal{O}[1/(E_{|\eta_2\rangle} - E_{|\eta_1\rangle})]$  by taking  $U^{(2)\dagger} U^{(1)\dagger} H_S U^{(1)} U^{(2)}$  with

$$U^{(2)} = \begin{pmatrix} 1 - \frac{1}{2} \left[ \left( \frac{t'_{L,R} \sin(\phi_S/2)}{\Delta E_{|S(002)\rangle}} \right)^2 + \left( \frac{t'_{L,R} \cos(\phi_S/2)}{\Delta E_{|S(011)\rangle}} \right)^2 \right] & \frac{t'_{L,R} \sin(\phi_S/2)}{\Delta E_{|S(002)\rangle}} & \frac{t'_{L,R} \cos(\phi_S/2)}{\Delta E_{|S(011)\rangle}} \\ \frac{t'_{L,R} \sin(\phi_S/2)}{\Delta E_{|S(002)\rangle}} & 1 - \left( \frac{t'_{L,R} \sin(\phi_S/2)}{\Delta E_{|S(002)\rangle}} \right)^2 & 0 \\ -\frac{t'_{L,R} \cos(\phi_S/2)}{\Delta E_{|S(011)\rangle}} & 0 & 1 - \left( \frac{t'_{L,R} \cos(\phi_S/2)}{\Delta E_{|S(011)\rangle}} \right)^2 \end{pmatrix}, \quad (\text{F12})$$

where

$$\delta E_{|S(002)\rangle} = E_{|S(002)\rangle} - E_{|S(101)\rangle} \quad (\text{F13a})$$

$$\begin{aligned}
&= \left( U_L - 2\varepsilon - \frac{t'_{L,M}}{2} \tan \phi_S \right) - (J_{L,R}^e + U'_{L,R}), \\
\delta E_{|S(011)\rangle} &= E_{|S(011)\rangle} - E_{|S(101)\rangle} \\
&= \left( J_{L,M}^e + U'_{L,M} + \Delta - \varepsilon + \frac{t'_{L,M}}{2} \tan \phi_S \right) - (J_{L,R}^e + U'_{L,R}).
\end{aligned} \tag{F13b}$$

The transformation  $U^{(2)\dagger} H^{(1)} U^{(2)}$  gives the ground eigenstate  $|S(101)\rangle'$ , whose explicit expression is

$$\begin{aligned}
|S(101)\rangle' &\approx \left[ 1 + \frac{1}{2} \left( \frac{t'_{L,M} \sin(\phi_S)}{\delta E_{|S(002)\rangle}} \right)^2 + \frac{1}{2} \left( \frac{t'_{L,M} \cos(\phi_S)}{\delta E_{|S(011)\rangle}} \right)^2 \right] |S(101)\rangle \\
&+ \frac{1}{2} (t'_{L,M} \sin \phi_S / 2) \left( \frac{1}{\delta E_{|S(002)\rangle}} - \frac{1}{\delta E_{|S(011)\rangle}} \right) |S(002)\rangle \\
&- \frac{t'_{L,M}}{2} \left( \frac{\sin^2(\phi_S)}{\delta E_{|S(002)\rangle}} + \frac{\cos^2(\phi_S)}{\delta E_{|S(011)\rangle}} \right) |S(011)\rangle,
\end{aligned} \tag{F14}$$

with eigenvalue

$$E_{|S(101)\rangle'} \approx (J_{L,R}^e + U'_{L,R}) - t'_{L,M} \sin^2(\phi_S) \left( \frac{t'_{L,M}}{\delta E_{|S(002)\rangle}} \right) - t'_{L,M} \cos^2(\phi_S) \left( \frac{t'_{L,M}}{\delta E_{|S(011)\rangle}} \right), \tag{F15}$$

where we only keep the terms up to  $\mathcal{O} [t'_{L,M}/(E_{|\eta_2\rangle} - E_{|\eta_1\rangle})]^2$  for  $|S(101)\rangle'$  while terms up to  $\mathcal{O} [t'^2_{L,M}/(E_{|\eta_2\rangle} - E_{|\eta_1\rangle})]$  for  $E_{|S(101)\rangle'}$ .  $E_{|S(101)\rangle'}$  is obtained explicitly by taking

$$E_{|S(101)\rangle'} \approx (J_{L,R}^e + U'_{L,R}) \tag{F16a}$$

$$+ t'_{L,M} \sin^2(\phi_S) \times \left[ \frac{1}{t'_{L,M} \sin^2(\phi_S)} \right] \tag{F16b}$$

$$\begin{aligned}
&\times \left( \langle S(101)|U^{(2)}|S(101)\rangle \langle S(101)|H_S^{(1)}|S(101)\rangle \langle S(101)|U^{(2)}|S(101)\rangle \right. \\
&+ \langle S(101)|U^{(2)}|S(002)\rangle \langle S(002)|H_S^{(1)}|S(101)\rangle \langle S(101)|U^{(2)}|S(101)\rangle \\
&+ \langle S(101)|U^{(2)}|S(101)\rangle \langle S(101)|H_S^{(1)}|S(002)\rangle \langle S(002)|U^{(2)}|S(101)\rangle \\
&\left. + \langle S(101)|U^{(2)}|S(002)\rangle \langle S(002)|H_S^{(1)}|S(002)\rangle \langle S(002)|U^{(2)}|S(101)\rangle \right)
\end{aligned}$$

$$+ t'_{L,M} \cos^2(\phi_S) \times \left[ \frac{1}{t'_{L,M} \cos^2(\phi_S)} \right] \tag{F16c}$$

$$\begin{aligned}
&\times \left( \langle S(101)|U^{(2)}|S(101)\rangle \langle S(101)|H_S^{(1)}|S(101)\rangle \langle S(101)|U^{(2)}|S(101)\rangle \right. \\
&+ \langle S(101)|U^{(2)}|S(011)\rangle \langle S(011)|H_S^{(1)}|S(101)\rangle \langle S(101)|U^{(2)}|S(101)\rangle \\
&+ \langle S(101)|U^{(2)}|S(101)\rangle \langle S(101)|H_S^{(1)}|S(011)\rangle \langle S(011)|U^{(2)}|S(101)\rangle \\
&\left. + \langle S(101)|U^{(2)}|S(011)\rangle \langle S(011)|H_S^{(1)}|S(011)\rangle \langle S(011)|U^{(2)}|S(101)\rangle \right),
\end{aligned}$$

where the first square bracket (Eq. (F16b)) indicates the contribution by the admixture with  $|S(002)\rangle$  while the second square bracket (Eq. (F16c)) indicates the contribution by the admixture with  $|S(011)\rangle$ . Since Eq. (F16) is equivalent to Eq. (F15) if only terms up to  $\mathcal{O} [t'^2_{L,M}/(E_{|\eta_2\rangle} - E_{|\eta_1\rangle})]$  are retained, we can rewrite  $E_{|S(101)\rangle'}$  as

$$E_{|S(101)\rangle'} \propto (J_{L,R}^e + U'_{L,R}) - t'_{L,M} \Phi_{|S(002)\rangle} - t'_{L,M} \Phi_{|S(011)\rangle}, \tag{F17}$$



where  $\Phi_{|\eta\rangle}$  indicates the magnitude of admixture between  $\eta$  and  $|S(101)\rangle$ .

Diagonalizing  $H_T$  (Eq. (F7b)) gives the ground eigenvector

$$|T(101)\rangle' = -\cos\frac{\Phi_T}{2}|T(101)\rangle + \sin\frac{\Phi_T}{2}|T(011)\rangle, \quad (\text{F18})$$

whose eigenvalue is

$$E_{|T(101)\rangle'} = (-J_{L,R}^e + U'_{L,R}) - \frac{t'_{L,M}}{2} \tan\Phi_{|T(011)\rangle}. \quad (\text{F19})$$

The admixture angle between  $|T(101)\rangle$  and  $|T(011)\rangle$ ,  $\Phi_{|T(011)\rangle}$ , is defined as

$$\tan\Phi_{|T(011)\rangle} = \frac{2t'_{L,M}}{U'_{L,M} + \Delta - U'_{L,R} - \varepsilon - (J_{L,M}^e - J_{L,R}^e)}. \quad (\text{F20})$$

Since  $\tan\Phi_{|T(011)\rangle} \approx \Phi_{|T(011)\rangle}$ ,  $E_{|T(101)\rangle'}$  can be rewritten as

$$E_{|T(101)\rangle'} \propto (-J_{L,R}^e + U'_{L,R}) - t'_{L,M}\Phi_{|T(011)\rangle}. \quad (\text{F21})$$

The condition  $\tan\Phi_{|T(011)\rangle} \approx \Phi_{|T(011)\rangle}$  is satisfied since  $\langle T(011)|T(101)\rangle' < 10^{-1}$ .

From Eq. (F17) and (F21), the superexchange energy  $J_{se}$  is

$$\begin{aligned} J_{se}(\Delta, \varepsilon \gg 0) &= E_{|T(101)\rangle'} - E_{|S(101)\rangle'} \\ &\approx -2J_{L,R}^e + t'_{L,M} \left[ \frac{t'_{L,M} \sin^2 \phi_S}{\delta E_{|S(002)\rangle}} + \frac{t'_{L,M} \cos^2 \phi_S}{\delta E_{|S(011)\rangle}} - \frac{1}{2} \tan\Phi_{|T(011)\rangle} \right] \\ &= -2J_{L,R}^e + J_{se(L,M)}^t(\Delta, \varepsilon \gg 0) \\ &\propto -2J_{L,R}^e + t'_{L,M} [\Phi_{|S(002)\rangle} + \Phi_{|S(011)\rangle} - \Phi_{|T(011)\rangle}], \end{aligned} \quad (\text{F22})$$

In the second line of Eq. (F22), we assume

$$\begin{aligned} \delta E_{\overline{|S(002)\rangle}} &\approx \delta E_{|S(002)\rangle} \\ &= E_{|S(002)\rangle} - E_{|S(101)\rangle} \\ &= (U_L - 2\varepsilon) - (J_{L,R}^e + U'_{L,R}), \end{aligned} \quad (\text{F23a})$$

$$\begin{aligned} \delta E_{\overline{|S(011)\rangle}} &\approx \delta E_{|S(011)\rangle} \\ &= E_{|S(011)\rangle} - E_{|S(101)\rangle} \\ &= (J_{L,M}^e + U'_{L,M} + \Delta - \varepsilon) - (J_{L,R}^e + U'_{L,R}), \end{aligned} \quad (\text{F23b})$$

since  $\delta E_{|\eta\rangle}$  appears in the denominators in  $J_{se}$  while  $t'_{L,M} \tan \phi_S/2 \ll (U_L - 2\varepsilon) - (J_{L,R}^e + U'_{L,R})$  and  $t'_{L,M} \tan \phi_S/2 \ll (J_{L,M}^e + U'_{L,M} + \Delta - \varepsilon) - (J_{L,R}^e + U'_{L,R})$ . In the third line of Eq. (F22), we denote the term with the prefactor  $t'_{L,M}$  as  $J_{se(L,M)}^t$  while the condition  $\varepsilon \gg 0$  is explicitly written for the variable  $\varepsilon$  to indicate this is only applicable for the case in which  $E_{|S(011)\rangle'} > E_{|S(002)\rangle'} > E_{|S(101)\rangle'}$ .

- 
- [1] D. Loss and D. P. DiVincenzo, Quantum computation with quantum dots, *Phys. Rev. A* **57**, 120 (1998).  
[2] D. P. DiVincenzo, D. Bacon, J. Kempe, G. Burkard, and K. B. Whaley, Universal quantum computation with the exchange interaction, *Nature* **408**, 339 (2000).  
[3] J. R. Petta, A. C. Johnson, J. M. Taylor, E. A. Laird, A. Yacoby, M. D. Lukin, C. M. Marcus, M. P. Hanson, and A. C. Gossard, Coherent manipulation of coupled electron spins in semiconductor quantum dots, *Science* **309**, 2180 (2005).  
[4] S. Foletti, H. Bluhm, D. Mahalu, V. Umansky, and A. Yacoby, Universal quantum control of two-electron spin quantum bits using dynamic nuclear polarization, *Nat. Phys.* **5**, 903 (2009).  
[5] E. A. Laird, J. M. Taylor, D. P. DiVincenzo, C. M. Marcus, M. P. Hanson, and A. C. Gossard, Coherent spin manipulation in an exchange-only qubit, *Phys. Rev. B* **82**, 075403 (2010).  
[6] K. C. Nowack, M. Shafiei, M. Laforest, G. E. D. K. Prawiroatmodjo, L. R. Schreiber, C. Reichl,

- W. Wegscheider, and L. M. K. Vandersypen, Single-shot correlations and two-qubit gate of solid-state spins, *Science* **333**, 1269 (2011).
- [7] J. Medford, J. Beil, J. M. Taylor, S. D. Bartlett, A. C. Doherty, E. I. Rashba, D. P. DiVincenzo, H. Lu, A. C. Gosard, and C. M. Marcus, Self-consistent measurement and state tomography of an exchange-only spin qubit, *Nat. Nanotechnol.* **8**, 654 (2013).
- [8] Z. Shi, C. B. Simmons, J. R. Prance, J. K. Gamble, T. S. Koh, Y.-P. Shim, X. Hu, D. E. Savage, M. G. Lagally, M. A. Eriksson, M. Friesen, and S. N. Coppersmith, Fast hybrid silicon double-quantum-dot qubit, *Phys. Rev. Lett.* **108**, 140503 (2012).
- [9] D. Kim, Z. Shi, C. B. Simmons, D. R. Ward, J. R. Prance, T. S. Koh, J. K. Gamble, D. E. Savage, M. G. Lagally, M. Friesen, S. N. Coppersmith, and M. A. Eriksson, Quantum control and process tomography of a semiconductor quantum dot hybrid qubit, *Nature* **511**, 70 (2014).
- [10] K. Eng, T. D. Ladd, A. Smith, M. G. Borselli, A. A. Kiselev, B. H. Fong, K. S. Holabird, T. M. Hazard, B. Huang, P. W. Deelman, I. Milosavljevic, A. E. Schmitz, R. S. Ross, M. F. Gyure, and A. T. Hunter, Isotopically enhanced triple-quantum-dot qubit, *Sci. Adv.* **1**, e1500214 (2015).
- [11] Y.-P. Shim and C. Tahan, Charge-noise-insensitive gate operations for always-on, exchange-only qubits, *Phys. Rev. B* **93**, 121410 (2016).
- [12] A. Sala and J. Danon, Exchange-only singlet-only spin qubit, *Phys. Rev. B* **95**, 241303 (2017).
- [13] M. Russ, J. R. Petta, and G. Burkard, Quadrupolar exchange-only spin qubit, *Phys. Rev. Lett.* **121**, 177701 (2018).
- [14] D. M. Zajac, A. J. Sigillito, M. Russ, F. Borjans, J. M. Taylor, G. Burkard, and J. R. Petta, Resonantly driven cnot gate for electron spins, *Science* **359**, 439 (2018).
- [15] T. F. Watson, S. G. J. Philips, E. Kawakami, D. R. Ward, P. Scarlino, M. Veldhorst, D. E. Savage, M. G. Lagally, M. Friesen, S. N. Coppersmith, M. A. Eriksson, and L. M. K. Vandersypen, A programmable two-qubit quantum processor in silicon, *Nature* **555**, 633 (2018).
- [16] M. J. Gullans and J. R. Petta, Protocol for a resonantly driven three-qubit toffoli gate with silicon spin qubits, *Phys. Rev. B* **100**, 085419 (2019).
- [17] A. Sigillito, J. Loy, D. Zajac, M. Gullans, L. Edge, and J. Petta, Site-selective quantum control in an isotopically enriched  $^{28}\text{Si}/\text{Si}_{0.7}\text{Ge}_{0.3}$  quadruple quantum dot, *Phys. Rev. Appl.* **11**, 061006 (2019).
- [18] N. W. Hendrickx, W. I. L. Lawrie, M. Russ, F. van Riggenlen, S. L. de Snoo, R. N. Schouten, A. Sammak, G. Scappucci, and M. Veldhorst, A four-qubit germanium quantum processor, *Nature* **591**, 580 (2021).
- [19] S. G. J. Philips, M. T. Mađzik, S. V. Amitonov, S. L. de Snoo, M. Russ, N. Kalhor, C. Volk, W. I. L. Lawrie, D. Brousse, L. Tryputen, B. P. Wuetz, A. Sammak, M. Veldhorst, G. Scappucci, and L. M. K. Vandersypen, Universal control of a six-qubit quantum processor in silicon, [arXiv:2202.09252](https://arxiv.org/abs/2202.09252).
- [20] J. M. Taylor, H. A. Engel, W. Dür, A. Yacoby, C. M. Marcus, P. Zoller, and M. D. Lukin, Fault-tolerant architecture for quantum computation using electrically controlled semiconductor spins, *Nat. Phys.* **1**, 177 (2005).
- [21] M. D. Shulman, O. E. Dial, S. P. Harvey, H. Bluhm, V. Umansky, and A. Yacoby, Demonstration of entanglement of electrostatically coupled singlet-triplet qubits, *Science* **336**, 202 (2012).
- [22] A. Pal, E. I. Rashba, and B. I. Halperin, Driven nonlinear dynamics of two coupled exchange-only qubits, *Phys. Rev. X* **4**, 011012 (2014).
- [23] A. Pal, E. I. Rashba, and B. I. Halperin, Exact cnot gates with a single nonlocal rotation for quantum-dot qubits, *Phys. Rev. B* **92**, 125409 (2015).
- [24] H.-O. Li, G. Cao, G.-D. Yu, M. Xiao, G.-C. Guo, H.-W. Jiang, and G.-P. Guo, Conditional rotation of two strongly coupled semiconductor charge qubits, *Nat. Commun.* **6**, 7681 (2015).
- [25] J. M. Nichol, L. A. Orona, S. P. Harvey, S. Fallahi, G. C. Gardner, M. J. Manfra, and A. Yacoby, High-fidelity entangling gate for double-quantum-dot spin qubits, *npj Quantum Inf.* **3**, 3 (2017).
- [26] M. A. Wolfe, F. A. Calderon-Vargas, and J. P. Kestner, Robust operating point for capacitively coupled singlet-triplet qubits, *Phys. Rev. B* **96**, 201307 (2017).
- [27] D. Buterakos, R. E. Throckmorton, and S. Das Sarma, Crosstalk error correction through dynamical decoupling of single-qubit gates in capacitively coupled singlet-triplet semiconductor spin qubits, *Phys. Rev. B* **97**, 045431 (2018).
- [28] S. F. Neyens, E. MacQuarrie, J. Dodson, J. Corrigan, N. Holman, B. Thorggrimsson, M. Palma, T. McJunkin, L. Edge, M. Friesen, S. Coppersmith, and M. Eriksson, Measurements of capacitive coupling within a quadruple-quantum-dot array, *Phys. Rev. Appl.* **12**, 064049 (2019).
- [29] G. X. Chan and X. Wang, Robust entangling gate for capacitively coupled few-electron singlet-triplet qubits, [arXiv:2201.01583](https://arxiv.org/abs/2201.01583).
- [30] P. Huang and X. Hu, Fast spin-valley-based quantum gates in si with micromagnets, *npj Quantum Inf.* **7**, 162 (2021).
- [31] P. Huang and X. Hu, Spin qubit relaxation in a moving quantum dot, *Phys. Rev. B* **88**, 075301 (2013).
- [32] X. Mi, J. V. Cady, D. M. Zajac, P. W. Deelman, and J. R. Petta, Strong coupling of a single electron in silicon to a microwave photon, *Science* **355**, 156 (2017).
- [33] X. Mi, J. V. Cady, D. M. Zajac, J. Stehlik, L. F. Edge, and J. R. Petta, Circuit quantum electrodynamics architecture for gate-defined quantum dots in silicon, *Appl. Phys. Lett.* **110**, 043502 (2017).
- [34] X. Mi, M. Benito, S. Putz, D. M. Zajac, J. M. Taylor, G. Burkard, and J. R. Petta, A coherent spin-photon interface in silicon, *Nature* **555**, 599 (2018).
- [35] D. J. van Woerkom, P. Scarlino, J. H. Ungerer, C. Müller, J. V. Koski, A. J. Landig, C. Reichl, W. Wegscheider, T. Ihn, K. Ensslin, and A. Wallraff, Microwave photon-mediated interactions between semiconductor qubits, *Phys. Rev. X* **8**, 041018 (2018).
- [36] J. V. Koski, A. J. Landig, M. Russ, J. C. Abadillo-Uriel, P. Scarlino, B. Kratochwil, C. Reichl, W. Wegscheider, G. Burkard, M. Friesen, S. N. Coppersmith, A. Wallraff, K. Ensslin, and T. Ihn, Strong photon coupling to the quadrupole moment of an electron in a solid-state qubit, *Nat. Phys.* **16**, 642 (2020).
- [37] F. Borjans, X. G. Croot, X. Mi, M. J. Gullans, and J. R. Petta, Resonant microwave-mediated interactions between distant electron spins, *Nature* **577**, 195 (2020).
- [38] G. Burkard, M. J. Gullans, X. Mi, and J. R. Petta, Superconductor-semiconductor hybrid-circuit quantum electrodynamics, *Nat. Rev. Phys.* **2**, 129 (2020).
- [39] F. Borjans, X. Croot, S. Putz, X. Mi, S. M. Quinn,

- A. Pan, J. Kerckhoff, E. J. Pritchett, C. A. Jackson, L. F. Edge, R. S. Ross, T. D. Ladd, M. G. Borselli, M. F. Gyure, and J. R. Petta, Split-gate cavity coupler for silicon circuit quantum electrodynamics, *Appl. Phys. Lett.* **116**, 234001 (2020).
- [40] B. Kratochwil, J. V. Koski, A. J. Landig, P. Scarlino, J. C. Abadillo-Uriel, C. Reichl, S. N. Coppersmith, W. Wegscheider, M. Friesen, A. Wallraff, T. Ihn, and K. Ensslin, Charge qubit in a triple quantum dot with tunable coherence, *Phys. Rev. Research* **3**, 013171 (2021).
- [41] R. Ruskov and C. Tahan, Modulated longitudinal gates on encoded spin qubits via curvature couplings to a superconducting cavity, *Phys. Rev. B* **103**, 035301 (2021).
- [42] T. Nakajima, M. R. Delbecq, T. Otsuka, S. Amaha, J. Yoneda, A. Noiri, K. Takeda, G. Allison, A. Ludwig, A. D. Wieck, X. Hu, F. Nori, and S. Tarucha, Coherent transfer of electron spin correlations assisted by dephasing noise, *Nat. Commun.* **9**, 2133 (2018).
- [43] T. Fujita, T. A. Baart, C. Reichl, W. Wegscheider, and L. M. K. Vandersypen, Coherent shuttle of electron-spin states, *npj Quantum Inf.* **3**, 22 (2017).
- [44] A. R. Mills, D. M. Zajac, M. J. Gullans, F. J. Schupp, T. M. Hazard, and J. R. Petta, Shuttling a single charge across a one-dimensional array of silicon quantum dots, *Nat. Commun.* **10**, 1063 (2019).
- [45] B. Buonacorsi, B. Shaw, and J. Baugh, Simulated coherent electron shuttling in silicon quantum dots, *Phys. Rev. B* **102**, 125406 (2020).
- [46] F. Ginzel, A. R. Mills, J. R. Petta, and G. Burkard, Spin shuttling in a silicon double quantum dot, *Phys. Rev. B* **102**, 195418 (2020).
- [47] B. Jadot, P.-A. Mortemousque, E. Chanrion, V. Thiney, A. Ludwig, A. D. Wieck, M. Urdampilleta, C. Bäuerle, and T. Meunier, Distant spin entanglement via fast and coherent electron shuttling, *Nat. Nanotechnol.* **16**, 570 (2021).
- [48] A. Noiri, K. Takeda, T. Nakajima, T. Kobayashi, A. Sammak, G. Scappucci, and S. Tarucha, A shuttling-based two-qubit logic gate for linking distant silicon quantum processors, [arXiv:2202.01357](https://arxiv.org/abs/2202.01357).
- [49] S. Bose, Quantum communication through an unmodulated spin chain, *Phys. Rev. Lett.* **91**, 207901 (2003).
- [50] A. Wójcik, T. Łuczak, P. Kurzyński, A. Grudka, T. Gdala, and M. Bednarska, Unmodulated spin chains as universal quantum wires, *Phys. Rev. A* **72**, 034303 (2005).
- [51] L. Campos Venuti, C. Degli Esposti Boschi, and M. Roncaglia, Long-distance entanglement in spin systems, *Phys. Rev. Lett.* **96**, 247206 (2006).
- [52] S. Bose, Quantum communication through spin chain dynamics: an introductory overview, *Contemp. Phys.* **48**, 13 (2007).
- [53] M. Friesen, A. Biswas, X. Hu, and D. Lidar, Efficient multiqubit entanglement via a spin bus, *Phys. Rev. Lett.* **98**, 230503 (2007).
- [54] S. Oh, M. Friesen, and X. Hu, Even-odd effects of heisenberg chains on long-range interaction and entanglement, *Phys. Rev. B* **82**, 140403 (2010).
- [55] S. Oh, L.-A. Wu, Y.-P. Shim, J. Fei, M. Friesen, and X. Hu, Heisenberg spin bus as a robust transmission line for quantum-state transfer, *Phys. Rev. A* **84**, 022330 (2011).
- [56] F. R. Braakman, P. Barthelemy, C. Reichl, W. Wegscheider, and L. M. K. Vandersypen, Long-distance coherent coupling in a quantum dot array, *Nat. Nanotechnol.* **8**, 432 (2013).
- [57] T. A. Baart, T. Fujita, C. Reichl, W. Wegscheider, and L. M. K. Vandersypen, Coherent spin-exchange via a quantum mediator, *Nat. Nanotechnol.* **12**, 26 (2017).
- [58] X. Croot, S. Pauka, J. Watson, G. Gardner, S. Fallahi, M. Manfra, and D. Reilly, Device architecture for coupling spin qubits via an intermediate quantum state, *Phys. Rev. Appl.* **10**, 044058 (2018).
- [59] F. K. Malinowski, F. Martins, T. B. Smith, S. D. Bartlett, A. C. Doherty, P. D. Nissen, S. Fallahi, G. C. Gardner, M. J. Manfra, C. M. Marcus, and F. Kuemmeth, Fast spin exchange across a multielectron mediator, *Nat. Commun.* **10**, 1196 (2019).
- [60] H. Qiao, Y. P. Kandel, K. Deng, S. Fallahi, G. C. Gardner, M. J. Manfra, E. Barnes, and J. M. Nichol, Coherent multispin exchange coupling in a quantum-dot spin chain, *Phys. Rev. X* **10**, 031006 (2020).
- [61] K. Deng and E. Barnes, Interplay of exchange and superexchange in triple quantum dots, *Phys. Rev. B* **102**, 035427 (2020).
- [62] K. W. Chan, H. Sahasrabudhe, W. Huang, Y. Wang, H. C. Yang, M. Veldhorst, J. C. C. Hwang, F. A. Mohiyaddin, F. E. Hudson, K. M. Itoh, A. Saraiva, A. Morello, A. Laucht, R. Rahman, and A. S. Dzurak, Exchange coupling in a linear chain of three quantum-dot spin qubits in silicon, *Nano Lett.* **21**, 1517 (2021).
- [63] H. Qiao, Y. P. Kandel, S. Fallahi, G. C. Gardner, M. J. Manfra, X. Hu, and J. M. Nichol, Long-distance superexchange between semiconductor quantum-dot electron spins, *Phys. Rev. Lett.* **126**, 017701 (2021).
- [64] J. Knörzer, C. J. van Diepen, T.-K. Hsiao, G. Giedke, U. Mukhopadhyay, C. Reichl, W. Wegscheider, J. I. Cirac, and L. M. K. Vandersypen, Long-range electron-electron interactions in quantum dot systems and applications in quantum chemistry, [arXiv:2202.06756](https://arxiv.org/abs/2202.06756).
- [65] E. Barnes, J. P. Kestner, N. T. T. Nguyen, and S. Das Sarma, Screening of charged impurities with multielectron singlet-triplet spin qubits in quantum dots, *Phys. Rev. B* **84**, 235309 (2011).
- [66] X. Wang, S. Yang, and S. Das Sarma, Quantum theory of the charge-stability diagram of semiconductor double-quantum-dot systems, *Phys. Rev. B* **84**, 115301 (2011).
- [67] R. Li, X. Hu, and J. Q. You, Controllable exchange coupling between two singlet-triplet qubits, *Phys. Rev. B* **86**, 205306 (2012).
- [68] U. Merkt, J. Huser, and M. Wagner, Energy spectra of two electrons in a harmonic quantum dot, *Phys. Rev. B* **43**, 7320 (1991).
- [69] M. Wagner, U. Merkt, and A. V. Chaplik, Spin-singlet-spin-triplet oscillations in quantum dots, *Phys. Rev. B* **45**, 1951 (1992).
- [70] K. Kim, S. Korenblit, R. Islam, E. E. Edwards, M.-S. Chang, C. Noh, H. Carmichael, G.-D. Lin, L.-M. Duan, C. C. J. Wang, J. K. Freericks, and C. Monroe, Quantum simulation of the transverse Ising model with trapped ions, *New J. Phys.* **13**, 105003 (2011).
- [71] R. Islam, E. E. Edwards, K. Kim, S. Korenblit, C. Noh, H. Carmichael, G. D. Lin, L. M. Duan, C. C. Joseph Wang, J. K. Freericks, and C. Monroe, Onset of a quantum phase transition with a trapped ion quantum simulator, *Nat. Commun.* **2**, 377 (2011).
- [72] R. Islam, C. Senko, W. C. Campbell, S. Korenblit, J. Smith, A. Lee, E. E. Edwards, C.-C. J. Wang, J. K.

- Freericks, and C. Monroe, Emergence and frustration of magnetism with variable-range interactions in a quantum simulator, *Science* **340**, 583 (2013).
- [73] M. Gärttner, J. G. Bohnet, A. Safavi-Naini, M. L. Wall, J. J. Bollinger, and A. M. Rey, Measuring out-of-time-order correlations and multiple quantum spectra in a trapped-ion quantum magnet, *Nat. Phys.* **13**, 781 (2017).
- [74] J. R. Schrieffer and P. A. Wolff, Relation between the anderson and kondo hamiltonians, *Phys. Rev.* **149**, 491 (1966).
- [75] J. Levy, Universal quantum computation with spin-1/2 pairs and heisenberg exchange, *Phys. Rev. Lett.* **89**, 147902 (2002).
- [76] M. D. Reed, B. M. Maune, R. W. Andrews, M. G. Borselli, K. Eng, M. P. Jura, A. A. Kiselev, T. D. Ladd, S. T. Merkel, I. Milosavljevic, E. J. Pritchett, M. T. Rakher, R. S. Ross, A. E. Schmitz, A. Smith, J. A. Wright, M. F. Gyure, and A. T. Hunter, Reduced sensitivity to charge noise in semiconductor spin qubits via symmetric operation, *Phys. Rev. Lett.* **116**, 110402 (2016).
- [77] F. Martins, F. K. Malinowski, P. D. Nissen, E. Barnes, S. Fallahi, G. C. Gardner, M. J. Manfra, C. M. Marcus, and F. Kuemmeth, Noise suppression using symmetric exchange gates in spin qubits, *Phys. Rev. Lett.* **116**, 116801 (2016).
- [78] X. Wu, D. R. Ward, J. R. Prance, D. Kim, J. K. Gamble, R. T. Mohr, Z. Shi, D. E. Savage, M. G. Lagally, M. Friesen, S. N. Coppersmith, and M. A. Eriksson, Two-axis control of a singlet-triplet qubit with an integrated micromagnet, *Proc. Natl. Acad. Sci. U.S.A.* **111**, 11938 (2014).
- [79] K. Takeda, A. Noiri, J. Yoneda, T. Nakajima, and S. Tarucha, Resonantly driven singlet-triplet spin qubit in silicon, *Phys. Rev. Lett.* **124**, 117701 (2020).
- [80] B. M. Maune, M. G. Borselli, B. Huang, T. D. Ladd, P. W. Deelman, K. S. Holabird, A. A. Kiselev, I. Alvarado-Rodriguez, R. S. Ross, A. E. Schmitz, M. Sokolich, C. A. Watson, M. F. Gyure, and A. T. Hunter, Coherent singlet-triplet oscillations in a silicon-based double quantum dot, *Nature* **481**, 344 (2012).
- [81] R. M. Jock, N. T. Jacobson, P. Harvey-Collard, A. M. Mounce, V. Srinivasa, D. R. Ward, J. Anderson, R. Manginell, J. R. Wendt, M. Rudolph, T. Pluym, J. K. Gamble, A. D. Baczewski, W. M. Witzel, and M. S. Carroll, A silicon metal-oxide-semiconductor electron spin-orbit qubit, *Nat. Commun.* **9**, 1768 (2018).
- [82] P. Harvey-Collard, R. M. Jock, N. T. Jacobson, A. D. Baczewski, A. M. Mounce, M. J. Curry, D. R. Ward, J. M. Anderson, R. P. Manginell, J. R. Wendt, M. Rudolph, T. Pluym, M. P. Lilly, M. Pioro-Ladrière, and M. S. Carroll, All-electrical universal control of a double quantum dot qubit in silicon mos, in *2017 IEEE International Electron Devices Meeting (IEDM)* (IEEE, New York, 2017) pp. 36.5.1–36.5.4.
- [83] R. Winkler, *Spin-orbit Coupling Effects in Two-Dimensional Electron and Hole Systems* (Springer, Berlin, 2003).
- [84] Q. Li, L. Cywiński, D. Culcer, X. Hu, and S. Das Sarma, Exchange coupling in silicon quantum dots: Theoretical considerations for quantum computation, *Phys. Rev. B* **81**, 085313 (2010).
- [85] G. Burkard, D. Loss, and D. P. DiVincenzo, Coupled quantum dots as quantum gates, *Phys. Rev. B* **59**, 2070 (1999).
- [86] O. E. Dial, M. D. Shulman, S. P. Harvey, H. Bluhm, V. Umansky, and A. Yacoby, Charge noise spectroscopy using coherent exchange oscillations in a singlet-triplet qubit, *Phys. Rev. Lett.* **110**, 146804 (2013).